Materials & Design 225 (2023) 111504

Contents lists available at ScienceDirect

Materials & Design

journal homepage: www.elsevier.com/locate/matdes

Plasticity of the C15-$CaAl_2$ Laves phase at room temperature

M. Freund [a,*], D. Andre [a], P.L. Sun [a], C.F. Kusche [a], S. Sandlöbes-Haut [a], H. Springer [b,c], S. Korte-Kerzel [a]

[a] Institute of Physical Metallurgy and Materials Physics, RWTH Aachen University, Germany
[b] Max-Planck-Institut für Eisenforschung GmbH, Düsseldorf, Germany
[c] Institute of Metal Forming, RWTH Aachen University, Aachen, Germany

HIGHLIGHTS

- We find that the {1 1 2} plane seems to be dominant for plasticity, although previous literature lists deformation on the {1 1 1} plane as the dominant mechanism for C15 Laves phases.
- We could quantify the CRSS for both slip systems, namely $\{111\}\langle 1\bar{1}0\rangle$ and $\{112\}\langle 1\bar{1}0\rangle$, as approximately the same at ~ 1 GPa.
- Our TEM investigations confirm the $[1\bar{1}0]$ Burgers vector type by using the g·b analysis.
- Together, these insights also allow us to explain why the crack and slip trace distribution around indentations varies systematically with crystal orientation.

GRAPHICAL ABSTRACT

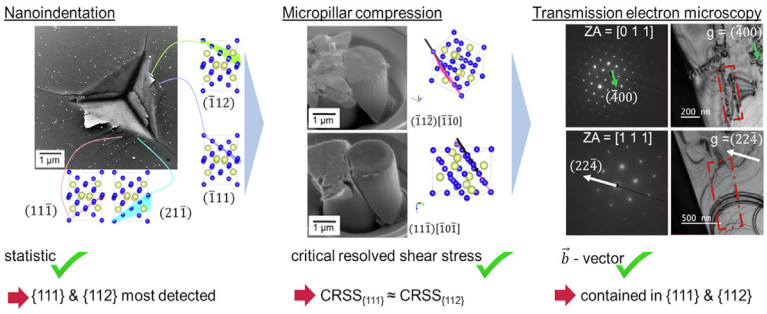

ARTICLE INFO

Article history:
Received 19 October 2022
Revised 2 December 2022
Accepted 12 December 2022
Available online 13 December 2022

Keywords:
Laves phases
$CaAl_2$
Plasticity
Electron microscopy
Nanoindentation
Micropillar compression

ABSTRACT

The room temperature plasticity of the cubic C15 $CaAl_2$ Laves phase was investigated using nanomechanical testing and electron microscopy. The correlation between slip traces in the vicinity of nanoindents and crystallographic orientation data allowed us to gain statistical data on the activated slip and crack planes for 10 different crystallographic orientations. Slip on {1 1 1} and {1 1 2} planes was found to be most favourable for all orientations, whereas cracks predominantly occurred on {1 1 2} planes. A constant hardness of 4.9 ± 0.7 GPa and an indentation modulus of 85.5 ± 4.0 GPa for all investigated orientations for a constant strain rate and a strain rate sensitivity of 0.028 ± 0.019 were measured. Micropillar compression tests and transmission electron microscopy confirmed slip on {1 1 1} and {1 1 2} planes with a Burgers vector of <1 1 0 > type. This allowed to determine the critical resolved shear stresses as 0.99 ± 0.03 GPa for {1 1 1}<1 1 0 > and 0.97 ± 0.07 GPa for {1 1 2}<1 1 0 > slip.

1. Introduction

Laves phases are a very common type of intermetallic compound, formed in many binary and ternary systems, as well as being "building blocks" of larger unit cells, such as in the μ-phase, which is a major precipitation phase in steels and superalloys [1,2]. Laves phases were discussed as the basis of future high temperature alloys, and have received recurring attention with a shifting focus on understanding their fundamental structure, stability and mechanical properties [3]. As topologically close packed phases (TCP) with the ideal composition AB_2 formed around an

* Corresponding author.
E-mail address: freund@imm.rwth-aachen.de (M. Freund).

https://doi.org/10.1016/j.matdes.2022.111504
0264-1275/

ideal ratio of the atomic diameters of $\sqrt{3/2}$, they are also being studied in colloids in the context of photonic crystals with a tunable bandgap [4] and to advance our understanding of amorphous and crystalline phase and defect formation [5,6].

The Laves phase $CaAl_2$ commonly occurs as precipitates in magnesium alloys containing Al and Ca. Despite its inherent brittleness, it can positively influence the plastic deformation of the magnesium alloys at room and moderately elevated temperatures and it is for this reason, and to widen our still limited knowledge about plastic deformation in these brittle crystals, that in this study the room temperature mechanical properties of the $CaAl_2$ Laves phase is investigated.

When Mg is alloyed with both Al and Ca, the Ca/Al ratio determines which intermetallic phase(s) are precipitated and their degree of interconnectivity formed in the magnesium matrix [7,8]. Recent work by Zubair et al. [9] revealed that, during tensile tests, a high interconnectivity provides a preferred growth path for cracks and thus promotes brittle failure, whereas a low connectivity results in an improved overall ductility. However, in creep testing [10], a higher degree of interconnectivity was found to yield an improvement of creep resistance as the intermetallic skeleton hinders dislocation motion [9]. A balance can therefore be struck by carefully choosing alloy composition and solidification conditions to balance sufficient ductility and improved creep resistance depending on the intended technical application. These promising results indicate that Laves phases are potential candidates to improve the creep strength of Mg-Al-alloys for applications above 150 °C, where the more commonly introduced $Mg_{17}Al_{12}$ phase becomes soft [11].

The intermetallic Laves phases formed in Mg-Al-Ca-alloys are the cubic $CaAl_2$ (C15 type), the hexagonal $CaMg_2$ (C14 type) and the hexagonal $Ca(Mg,Al)_2$ (C36 type) phases. The cubic $CaAl_2$ phase is characterised by its high melting temperature (1079 °C for the $CaAl_2$ phase as compared to 715 °C for the $CaMg_2$ phase [12]) and its high creep resistance compared to the hexagonal phases [12]. Creep tests at various temperatures by indentation with a Vickers indenter tip on the $CaAl_2$ phase have shown that for a holding time of 30 s, the microhardness only decreased moderately, from 402 HV to 318 HV and respectively, for a holding time of 3600 s, from 356 HV to 294 HV, with a temperature increase of 280 K from homologous temperatures,T_H, of 0.6 to 0.71 $\cdot T_m$ (T_m=melting temperature in K). In contrast to this, a more pronounced decrease in hardness could be observed for the hexagonal $CaMg_2$ phase showing a decreasing hardness from 156 HV to 47 HV for a 30 s holding period and 149 HV to 10 HV for 3600 s at the same temperature difference [12].

Due to the topologically closed packed structure of Laves phases, plasticity at ambient temperature is mostly impeded, leading to a gap of knowledge regarding mechanisms of plasticity at temperatures below the brittle-to-ductile transition temperature (BDTT), which was measured for Laves phases lying approximately between 60 and 71 % of the melting temperature [13–17]. Therefore, most of the previous literature has investigated Laves phases in temperature ranges above the BDTT, since macroscopic experimental setups can only introduce plasticity in this temperature regime. We summarise these studies on the deformation mechanisms of several cubic C15 Laves phases in the next section.

A theoretical approach of the deformation behaviour of Laves phases by Krämer et al. [16] revealed dislocation motion on the {1 1 1} plane with $\frac{1}{2}\langle 1\,1\,0\rangle$ perfect dislocations or $\frac{1}{6}\langle 1\,1\,2\rangle$ partial dislocations. Furthermore, possible dislocation motion without dissociation on the {1 0 1} plane with $\langle 0\,1\,0\rangle$ perfect dislocations and $\frac{1}{4}\langle 1\,2\,1\rangle$ dislocations for the cubic Laves phase was observed. Macroscopic, experimental tests led to similar results as predicted by Krämer for deformation above the BDTT. Studies on the $MgCu_2$ phase found that in addition to the {1 1 1} plane, the {1 1 0} and {1 0 0}-planes may act as additional slip planes (380–660 °C, 0.48–0.83 $\cdot T_m$) [18]. In a temperature range of 400–725 °C, 0.50–0.91$\cdot T_m$, other than the (1 1 1)[1 1 0] slip system, the (1 1 1)[1 1 2] twinning system was found [19]. Mechanical twinning was also the most frequently detected deformation mechanism for HfV_2 and HfV_2 + Nb for room temperature (RT), 0.02$\cdot T_m$, deformation tests [20,21]. Furthermore, perfect dislocations on the {1 1 1} plane with $\frac{1}{2}\langle 1\,0\,1\rangle$ were found in Fe_2(Dy,Tb) ($\geq$875 °C, $\geq$ 0.7 $\cdot T_m$), HfV_2 +-Nb (RT) and $NbCr_2$ (1300–1400 °C, 0.75–0.81 $\cdot T_m$), while $NbCr_2$ (1300–1400 °C) also showed dislocations on {1 1 1} planes dissociating into two $\frac{1}{6}\langle 1\,1\,2\rangle$ Shockley partials [20–24].

Experiments at room temperature were done using micropillar compression tests to suppress cracking below the BDTT [25], so that beside the slip system, critical resolved shear stresses (CRSS) for the observed slip systems could be identified. Micropillar compression studies of $NbCr_2$ and $NbCo_2$ revealed slip on the $\{1\,1\,1\}\langle 1\,1\,0\rangle$ slip system for both, with a CRSS of 4.6 GPa for orientations aligned for single slip and 4.4 GPa ($NbCr_2$) and 3.0–3.1 ± 0.7 GPa ($NbCo_2$) for orientations aligned for multiple slip [25–27]. Moreover, Korte et al. [28] and Luo et al. [29] found both the activation of the $\{111\} < 1\,\bar{1}\,0 >$ slip system for $NbCo_2$ and reported a CRSS of 3.1 ± 0.7 GPa and 3.2 ± 0.7 GPa, while Lou et al. [29] also observed the dislocation motion in the $< 11\,\bar{2} >$ direction on {1 1 1} planes with nearly the same CRSS of 3.0 ± 0.8 GPa.

The underlying mechanism by which deformation in Laves phases on these slip systems is often reported to occur is the so-called synchroshear mechanism on crystallographic planes containing the characteristic triple layer of Laves phases. The triple layer lies parallel to the {1 1 1} plane in the cubic C15 and parallel to the basal plane in the hexagonal C14 and C36 phases, and also related intermetallic phases containing Laves phase elements [30–35]. This mechanism is associated with local phase transformations from the hexagonal C14 or C36 to the cubic C15 phase after macroscopic compression tests [36–39], in which case it enables the transition by a simple restacking along the basal plane to create the different packings of these phases. The synchroshear mechanism consists of a synchronous movement of two neighbouring partial dislocations on a triple layer and essentially reverses the stacking direction within the triple layer, giving a local transformation between the prototypical phases or rather forming a stacking fault within the parent structure that corresponds to one of the other structures [30–32].

As seen above, the application of new testing methods on the nanoscale, such as nanoindentation and micropillar compression, now allows us to introduce plasticity in brittle materials below the BDTT. Here, we exploit these methods in conjunction with conventional transmission electron microscopy (TEM) analysis in order to gain a deeper understanding of the mechanisms governing plasticity in Laves phases. For the Mg-Al-Ca system, the hexagonal C14 Laves phase has already been characterised up to a temperature of 250 °C and, interestingly, non-basal slip was found to be predominant at all temperatures in addition to basal slip along the triple layer [40,41]. In contrast, the low temperature deformation behaviour of the cubic C15 is still to be unraveled, especially the qualitative and quantitative determination of the modulus, hardness, the rate dependence and activated slip systems. With this study, we aim to close this gap of knowledge by means of a statistical analysis of slip and crack planes around indentation deformation zones and evaluate possible slip systems and their critical resolved stresses by micropillar compression tests. To achieve a detailed insight into the underlying slip systems and mechanisms, further conventional TEM was used.

2. Experimental methods

2.1. Synthesis and microstructure characterisation

The as-cast samples of nominal $CaAl_2$ composition underwent an annealing procedure in a glass tube furnace under argon atmosphere at 600 °C for 24 h to ensure a homogeneous elemental distribution and obtain grain sizes in the range of a few hundred micrometers. Metallographically the samples were prepared as described in more detail in a previous publication [42]. In a first step, the samples were ground using SiC paper with a grit size of 1200 to 4000, followed by mechanical polishing steps with diamond paste from 6 μm down to 0.25 μm and ethanol with 5 % Polyethylene Glycol 400 (PEG) as a lubricant. A final oxide polishing with a grain size of 0.04 μm and cleaning step with soap and water followed.

Backscattered electron (BSE) imaging in a scanning electron microscope (SEM) (Helios Nanolab 600i, FEI, Eindhoven, NL) at an acceleration voltage of 5 kV revealed a two-phase microstructure with a matrix phase and a secondary phase surrounding the matrix phase (Fig. 1). Additionally, energy dispersive X-ray spectroscopy (EDX) measurements were performed in order to reveal the local chemical composition of the microstructure constituents, by calculating the chemistry over at least 34 point-measurements for both phases. The composition of the matrix phase was found to be 66.5 ± 2.5 at.-% Al and 33.6 ± 1.3 at.-% Ca, which corresponds well to the ideal stoichiometric composition of the $CaAl_2$ phase. The secondary phase consisted of 80.2 ± 1.1 at.-% Al and 19.8 ± 1.0 at.-% Ca and is thus attributed to the $CaAl_4$ phase.

The use of electron backscatter diffraction (EBSD) imaging (Helios Nanolab 600i, FEI, Eindhoven, NL) at an accelerating voltage of 20 kV and a current of 5.5 nA allowed us to identify the grain orientations of the cubic $CaAl_2$ phase, whereas for the tetragonal $CaAl_4$ phase, indexing was not possible because of diffuse Kikuchi patterns. This data was further analysed using orientation imaging microscopy (OIM) analysis™ (EDAX Inc.) in order to obtain the Schmid factors for certain slip systems of the $CaAl_2$ grains used for micropillar compression.

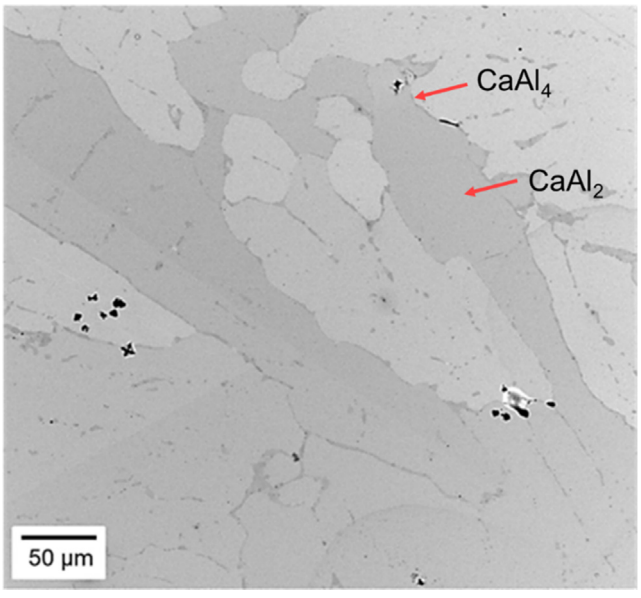

Fig. 1. Backscatter electron image of the microstructure recorded at an acceleration voltage of 5 kV. The matrix phase corresponds to the C15 $CaAl_2$ phase while the surrounding corresponds to the $CaAl_4$ phase.

2.2. Nanoindentation experiments

Nanomechanical tests were performed using an iNano nanoindenter (Nanomechanics Inc., TN, USA) with a diamond Berkovich tip (supplied by Synton MDP, Switzerland) and a dynamic indentation unit (continuous stiffness measurement (CSM)). Prior to testing, the diamond area function (DAF) of the indenter tip was calibrated according to the Oliver and Pharr method [43]. All nanomechanical tests were conducted in the $CaAl_2$ matrix phase at least 10 μm away from the $CaAl_4$ phase [44]. The first nanoindentation tests were performed with a constant strain rate of 0.2 s^{-1} up to a maximum depth of 500 nm. Before unloading, the indenter had a holding period of 2 s. These experiments were analysed for the hardness and indentation modulus as well as for slip traces in the vicinity of the nanoindents. This was done for a total of 120 nanoindents with 890 slip traces in 10 different crystal orientations by correlating the information from EBSD results and secondary electron (SE) images of the indents, as shown in [45].

Furthermore, strain rate jump tests (SRJT) in two different orientations were conducted based on the method first mentioned by Maier-Kiener et al. [46–48] to evaluate the strain rate sensitivity and activation volume of the $CaAl_2$ phase. These were performed at different strain rates of 0.1 s^{-1}, 0.04 s^{-1}, 0.1 s^{-1} and 0.01 s^{-1} with jumps taking place every 100 nm starting at 100 nm indentation depth.

2.3. Micropillar compression experiments

A total number of 15 micropillars with an aspect ratio of approximately 2.5 (pillar top diameter 2.1 μm/ pillar height 5.2 μm) was milled in seven differently oriented grains using focused ion beam (FIB) (Helios Nanolab 600i, FEI, Eindhoven, NL) milling. The compression tests were performed in-situ using an InSEM nanoindenter (Nanomechanics Inc., TN, USA) in an SEM (CLARA, Tescan, Brno, Czech Republic) with an approximate strain rate up to the onset of yielding of 0.1 s^{-1} and were manually stopped when a large strain burst was observed. Post-mortem SE images of the micropillars were taken under a 45° tilt angle using an acceleration voltage of 5 kV and a beam current of 0.69nA. This allowed us to identify the slip planes and potential slip directions for each micropillar. The obtained mechanical data was further corrected for elastic sink deformation of the tip and substrate using the Sneddon correction [49]. Subsequently, the stress at the initial strain burst was converted to the critical resolved shear stress (CRSS) for each slip system.

2.4. TEM experiments

Two TEM lamellae were cut out from indents using site specific FIB milling. The lamellae were then analysed using a JEOL JEM-F200 TEM under different two-beam conditions at 200 kV. A $g \cdot b$ extinction analysis, with g being the diffraction vector and b being the Burgers vector allowed us to identify the Burgers vectors of the dislocations.

3. Results

In order to unravel the mechanical properties and activated slip systems of the $CaAl_2$ phase at ambient temperature, several nanomechanical testing methods were applied: (I) nanoindentation tests to obtain the hardness and indentation modulus, (II) strain rate jump tests in order to determine the strain rate sensitivity and activation volume, (III) slip trace analysis in the vicinity of indents in order to gain a statistical measure of the activated slip systems and (IV) micropillar compression tests to identify the slip

planes and calculate the CRSS values using also information from (V) a consecutive TEM analysis, to determine the Burgers vectors of the introduced dislocations from the nanomechanical experiments.

3.1. Nanoindentation

The hardness and indentation modulus were calculated from a continuous stiffness measurement between 350 and 500 nm indentation depth and resulted in an average hardness of 4.9 ± 0.7 GPa and an average indentation modulus of 85.5 ± 4.0 GPa over all 10 orientations, using a constant Poisson ratio of 0.3. A representative load-indentation depth curve is given in Fig. 2. All load-indentation depth curves exhibit serrations, which became more pronounced with higher indentation depths.

Fig. 3 displays the results of the strain rate jump tests, showing a representative curve of the hardness change over the indentation depth with varying strain rate. The average hardness of 5.8 ± 0.8 GPa for the strain rate jump tests agrees, within the standard deviations, with the measured values at the constant strain rate of 0.2 s^{-1}. The averaging over depth for the strain rate jump tests was done over a depth range of 100 – 500 nm, including all measured strain rates. For all orientations, the first jump was conducted at approximately 100 nm followed by strain rate jumps (0.1 s^{-1}; 0.04 s^{-1}; 0.1 s^{-1}; 0.01 s^{-1}) every 100 nm. For the second jump, the hardness increased slightly whereas it decreased between 200 and 300 nm at the next jump to slower strain rates.

From this change in hardness with strain rate, the strain rate sensitivity (m) and the activation volume (V) can be calculated [46–48,50].

The strain rate sensitivity can be calculated based on equation (1):

$$m = \frac{d(\ln H)}{d(\ln \dot{\varepsilon})} \tag{1}$$

with H the hardness and $\dot{\varepsilon}$ the strain rate. The activation volume can then be calculated as

$$V = \frac{3\sqrt{3}\ k\ T}{m\ H} \tag{2}$$

with k the Boltzmann constant and T the absolute temperature in K.

The calculation of the strain rate sensitivity was performed by evaluating the hardness change at the jumps, taking a total amount of 600 values, 300 before and 300 after each hardness jump into account, and calculating the slope of these hardness data before and after the jump. With the extension of these linear trends from each strain rate increment, the hardness difference could be measured at the point of rate change to calculate the strain rate sensitivity. This led to an average strain rate sensitivity of 0.028 ± 0.019 and an activation volume of 0.530 ± 0.780 nm^3, corresponding to 3.75 ± 1.15 b^3, calculated with a lattice parameter of 0.80428 nm and a Burgers vector along the closed packed direction $\frac{a}{2}\langle 110\rangle$ (b = 0.5685 nm).

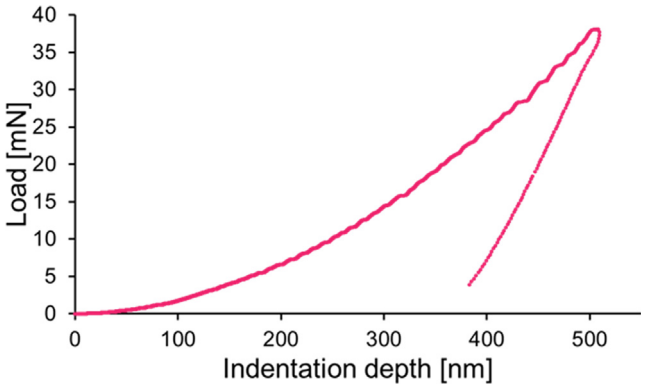

Fig. 2. Representative nanoindentation load-indentation depth curve at a constant strain rate of 0.2 s^{-1} to a maximum depth of 500 nm.

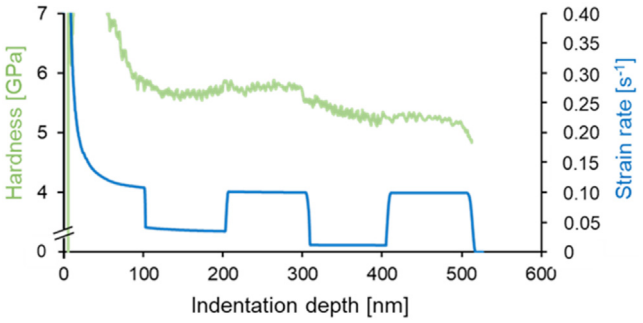

Fig. 3. Hardness and strain rate values over indentation depth for the $CaAl_2$ phase. The strain rate jump test (SRJT) was performed at different strain rates of 0.1 s^{-1}, 0.04 s^{-1}, 0.1 s^{-1}, 0.01 s^{-1}, which was varied every 100 nm.

3.2. Slip line analysis

The slip line analysis was performed on 120 indents, corresponding to 10 different crystallographic orientations. The evaluated indents were performed with a constant strain rate. For all investigated indents, at least one crack was observed to initiate from one of the indent corners, whereas not all indents were surrounded by visible slip lines.

For the slip line analysis, a MatLab® Code was used [45], which, together with the orientation data gained from EBSD measurements, (semi)automatically identified the most probable slip plane from SEM images. For this procedure, a tolerance angle of 3° between the measured angle of the slip trace with the horizontal and the identified plane was chosen. Due to the only small angular deviation in the plane of the sample surface between the {1 1 1} and {1 1 2} planes for some orientations, the automatic analysis has been manually corrected as described in [45] where the angle between both planes was found to be smaller than 3°. If more than one slip plane was assigned to the occurring slip plane, both possibilities were counted, so that the overall activation frequency in this case amounts to more than 100 %. The slip traces around the indents were then subdivided into three categories according to their morphology, namely lines, edges and curves, as suggested by Schröders et al. [51] (Fig. 4). All grain orientations are displayed in Fig. 4 within the inverse pole figure (IPF) map with a colour code visualising the morphology of the surface traces and those orientations in which only cracks were observed. As each indent for which slip traces were observed also had at least one adjacent crack, they were not included as an additional category in Fig. 4.

Fig. 5 displays examples of the slip trace analysis. For the identification of slip planes only straight lines and edges were used.

A total of 890 surface traces, including slip lines and cracks formed around a total of 120 indentations, were evaluated in order to obtain a statistical analysis. 625 of these surface traces pertain to plastic deformation and 265 to cracks, both were analysed separately. The corresponding results are depicted in Fig. 6. For the plastic deformation, 58 % of the resulting slip traces were correlated to {1 1 1} planes, followed by the {1 1 2} planes with an activation frequency of 48 % (the total activation frequency reaches over 100 % as a result of double counting of slip planes when the angle of different candidate slip planes is less than 3°). For the cracks, ori-

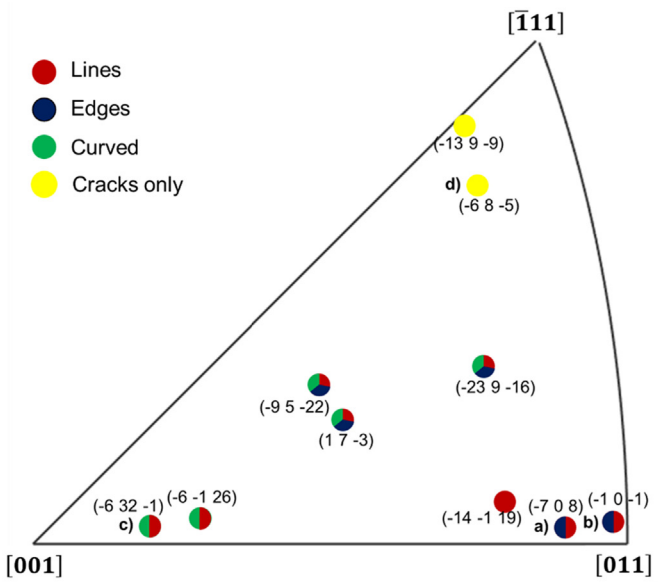

	{111}	{112}	{110}	{100}
(-13 9 -9)	0.35	0.40	0.29	0.50
(-6 8 -5)	0.38	0.35	0.32	0.50

	{111}	{112}	{110}	{100}
(-23 9 -16)	0.35	0.49	0.45	0.47
(1 7 -3)	0.35	0.43	0.35	0.22
(-9 5 -22)	0.48	0.46	0.44	0.37

	{111}	{112}	{110}	{100}
(-1 0 -1)	0.41	0.48	0.41	0.35
(-7 0 8)	0.47	0.33	0.43	0.35
(-14 -1 19)	0.47	0.19	0.45	0.35

	{111}	{112}	{110}	{100}
(-6 32 -1)	0.46	0.49	0.39	0.15
(-6 -1 26)	0.49	0.49	0.35	0.16

Fig. 4. Orientations of all analysed grains for slip line analysis as an inverse pole figure map with corresponding morphology of surface traces, such as in the publication of Schröders et al. [51], see Fig. 5 for images of the different morphologies here. All indents contain cracks, but with yellow, the orientation is shown, where only cracks were observed, red shows straight slip lines, blue edges and green rounded surface traces. The orientations labelled (a), (b), (c) and (d) are shown in a detailed slip line analysis in the corresponding subfigures of Fig. 5. Additionally, the highest Schmid factor for each slip system is given in the table. The Schmid factors were calculated by assuming uniaxial compression. (For interpretation of the references to colour in this figure legend, the reader is referred to the web version of this article.)

entations along {1 1 2} and {1 1 0} planes were mostly detected with 37 % and 28 %, respectively. 4 % of slip planes and 19 % of crack planes could not be assigned to any plane. The comparatively high number of not indexed crack planes results from the curved crack path and the changing morphology along the crack, which may nucleate at small depths and progress outwards as the indent is pushed further into the surface. In contrast, slip traces form and are successively flattened by the proceeding indentation, so that only the final traces remain visible outside the contact zone.

3.3. Micropillar compression

A total of 15 micropillars corresponding to 7 different orientations were deformed until strain bursts occurred. Representative micropillars for each orientation are depicted in Fig. 7 a) including their correspondingly oriented unit cells (Fig. 7 b)) and the engineering stress strain curves (Fig. 8). For slip plane determination, the 45° tilted SE-images of the micropillar were compared to the 90° tilted unit cell taken from VESTA, to realise the side view [52]. The slip angles of both images were compared taking the tilt during imaging of 45° into account using $\gamma_{90} = \tan^{-1}\left(\tan(\gamma_{45}) \cdot \sqrt{2}\right)$. The corresponding slip planes were again assigned with a tolerance of ± 3°. For the slip direction the best fitting slip plane and Burgers vector with the highest Schmid factor were assumed. The slip planes found to show deviation angles of $\leq 3°$ were the {1 1 1} and {1 1 2} slip planes. The distinction of these planes was not as difficult as in the slip plane analysis of the deformation zone around indents, as the angular difference was more clearly visible in the geometry of a micropillar.

The CRSS was determined by taking the engineering stress, at the point at which the first strain burst happened, multiplied with the Schmid factor of the determined slip system.

All compressed micropillars are listed in Table 1 including their identified slip systems, Schmid factors (m_S), compression axes, yield stresses (σ_y) and CRSS values.

Overall, 10 of the 15 pillars slipped on the {1 1 1} planes and 5 on the {1 1 2} planes. Slip on the {1 1 1}<1 $\bar{1}$ 0 > slip systems occurred at an average yield stress of 2.96 ± 0.54 GPa resulting in an average CRSS of 0.99 ± 0.07 GPa (Table 1), whereas slip on the {1 1 2}<1 $\bar{1}$ 0 > slip systems occurred at a yield stress ranging from 2.67 GPa to 3.69 GPa resulting in an average of 2.94 ± 0.24 GPa and an average CRSS value of 0.97 ± 0.03 GPa (Table 1). The error is given as the standard deviation for the specific slip systems.

For micropillar 13 and 14, the CRSS could not be determined unambiguously, and is therefore marked with a "*" in Table 1 and not included in the average values given above. This is due to the activation of two slip systems and the impossibility of assigning the strain bursts to one of the slip systems. Fig. 9 depicts the slip events observed for pillar 13. From the front (Fig. 9 a)), only one slip system, $\left(\bar{1}\,2\,1\right)\left[\bar{1}\,0\,\bar{1}\right]$, is visible, whereas in the back view (Fig. 9 b)), two slip systems are visible, both belonging to the {1 1 2} <1 $\bar{1}$ 0 > slip system.

In Table 2 all measured mechanical properties and their corresponding values are listed.

3.4. TEM

For TEM analysis, a site-specific lamella was lifted out from an indent for which the {1 1 1} and {1 1 2} planes could not be distinguished by surface analysis alone. Fig. 10 a) displays the alignment of the lamella, where letters "A" and "B" represent the two sides of the lamella. Additionally, the possible slip planes, $(1\,1\,\bar{1})$, $(2\,1\,\bar{1})$, $(\bar{1}\,1\,1)$ and $(\bar{2}\,1\,1)$, determined by the slip line analysis are shown in the unit cells. In Fig. 10 b), a scanning transmission electron microscopy (STEM) image of the deformation zone is shown. Some clear lines next to the indent at the "A" side are observed to go from the bulk material to the surface. In addition, the surface slip traces were assigned to be the edged lines on the surface and thus correlated to ductile deformation. Looking at the deformation zone below the indentation, cracks can be seen emanating from these edged slip lines.

Fig. 10(c) displays a bright field (BF) TEM image taken along the [1 1 2] zone axis. It can be seen that the deformed microstructure is

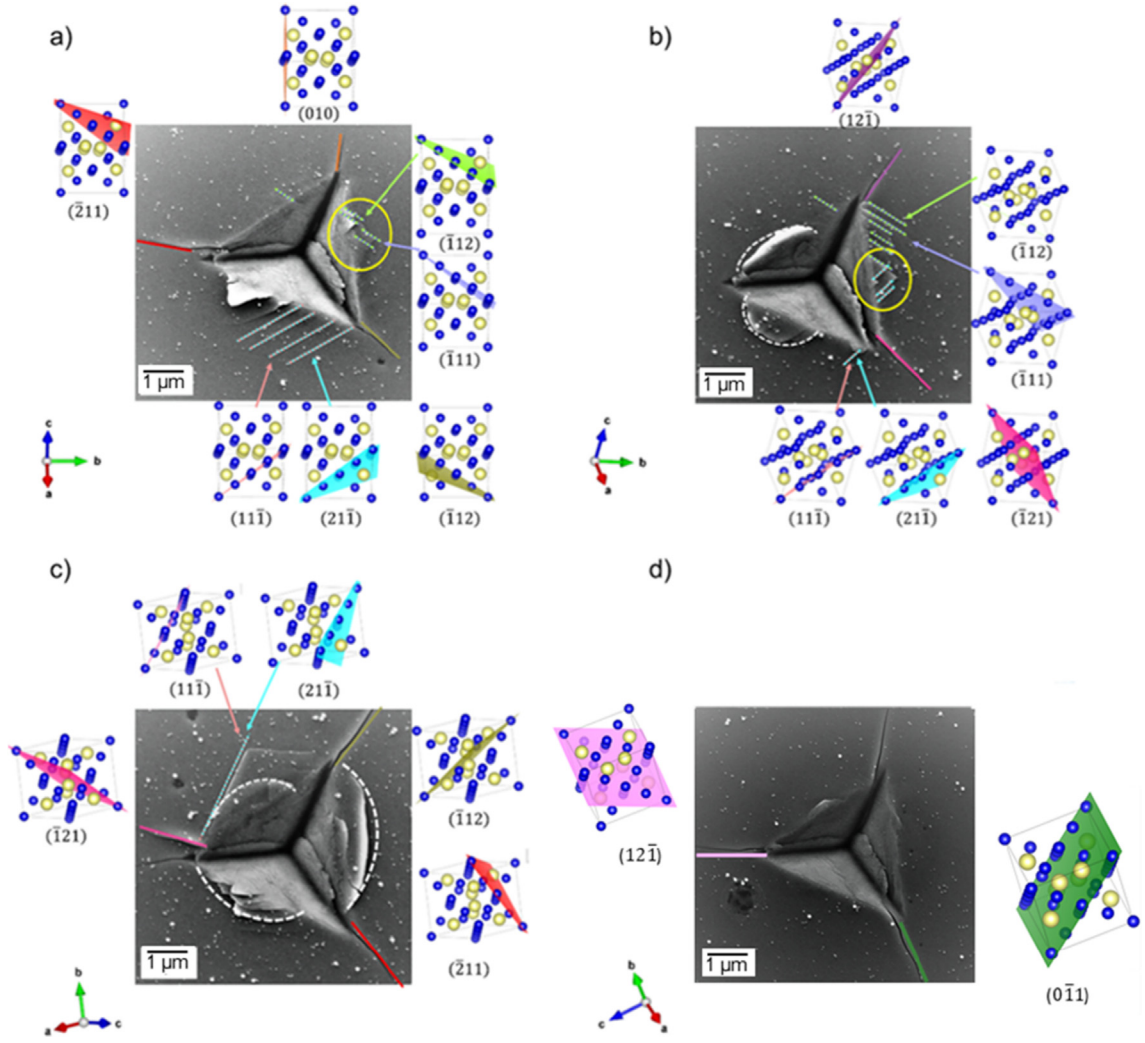

Fig. 5. Examples of the representation of the slip trace analysis for four different orientations: The traces in the vicinity of the indent are subdivided into the following categories depending on their morphology: straight slip lines (correlated with their slip plane in the $CaAl_2$ phase using VESTA (Visualization for Electronic and Structural Analysis [52])), edges marked by yellow circles, and curved lines indicated by white dotted curved lines. The latter were not further analysed. Next to the SE images in a-d), the top view on the correspondingly orientated $CaAl_2$ unit cell including the observed slip planes is depicted. The compression axes are a) $(\bar{7}\,0\,8)$, b) $(\bar{1}\,0\,\bar{1})$, c) $(\bar{6}\,32\,\bar{1})$ and d) $(\bar{6}\,8\,\bar{5})$. (For interpretation of the references to colour in this figure legend, the reader is referred to the web version of this article.)

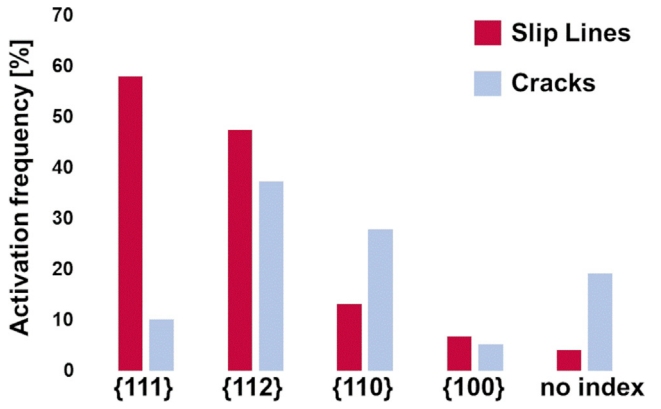

Fig. 6. Activation frequency of the slip and crack planes in the vicinity of the analysed nanoindents.

not homogeneous. The dislocation density is high under the indent, which indicates the occurrence of large plastic deformation. Multiple slip systems should have been activated under the indent. The dislocation density is observed to decrease away from the indent. Slightly away from the indent, deformation is confined within some bands, which will be named "slip bands" in the following sections. At least two sets of slip bands appear in this area. Further away from the indent, only one set of slip band is observed. However, the finding that dislocations with different Burgers vectors exist in the same slip band, makes it more difficult to index the dislocations' Burgers vectors. This is discussed in more detail below. Similarly, it is noted that horizontally away from the indent, in the area of low dislocation density, some slip bands can be more clearly observed and are indicated by white dotted lines in Fig. 10 c). In order to determine the orientations of these slip bands, the lamella was further tilted to the [0 1 1] zone axis and the slip bands on both "A" and "B" sides are determined to be $(2\,\bar{1}\,1)$ and $(21\,\bar{1})$ plane traces, respectively. These slip bands are also observed to lie parallel to the straight crack planes. Moreover, the blue dotted rectangle represents the area where slip bands were observed lying also on the $(2\,\bar{1}\,1)$ plane (Fig. 10), which also can be seen in more detail in Fig. 11. Within the red dotted rectangle, the region where the Burgers vector was analysable is marked (in more detail Fig. 12), also the yellow rectangle signs the area,

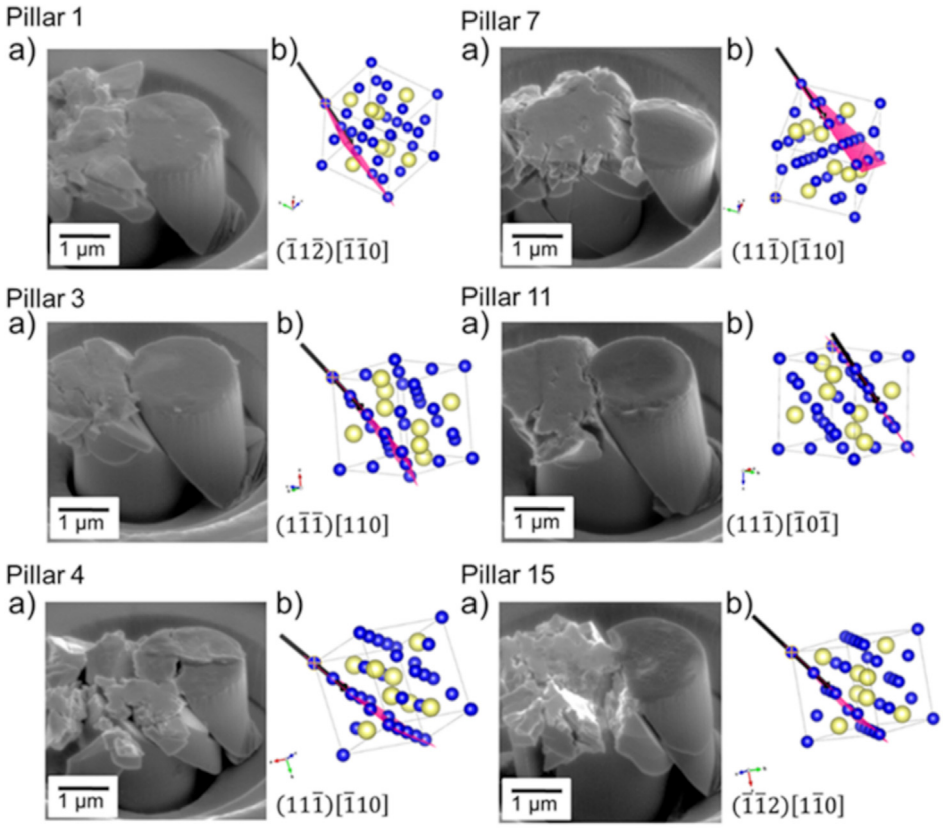

Fig. 7. Images and crystal orientation for selected micropillars. a) SE-images of the deformed micropillars taken under a tilt angle of 45°, b) the correspondingly oriented unit cell including the identified slip plane and the possible slip direction under 90° tilt angle using VESTA [52].

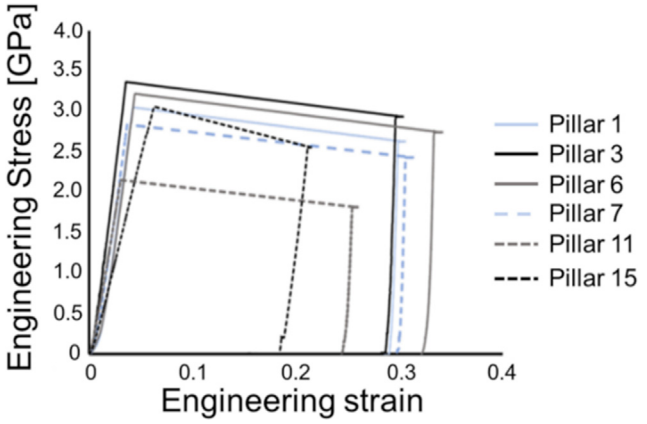

Fig. 8. Engineering stress - engineering strain curves of the deformed micropillars shown in Fig. 7.

where structures can be observed, which can be interpreted as stacking faults (Fig. 13).

Especially the evidence of dislocations on a {1 1 2} plane was found by rotating the lamella around 180°, shown in Fig. 11, where slip bands lie parallel to the $(\bar{2}\,1\,\bar{1})$.

In the area away from the indent marked by a red rectangle in Fig. 10 c), two slip bands with a high dislocation density were observed and either one or two sets of dislocations were noticed within these two slip bands. These two slip bands were further analyzed under different two-beam conditions (Fig. 12). The left slip band includes two different parallel dislocation sets lying antiparallel to each other and including an intersection. Both slip bands were evaluated in more detail for Burgers vector analysis. For this, dislocations within these slip bands were observed after tilting to three different zone axes namely [0 1 1], [1 1 2] and [1 1 1], and six different two-beam conditions, g = $(\bar{3}\,1\,1)$, g = $(\bar{3}\,1\,\bar{1})$, g = $(\bar{1}\,3\,\bar{1})$, g = $(\bar{2}\,2\,0)$, g = $(2\,2\,\bar{4})$ and g = $(\bar{2}\,\bar{2}\,2)$ were applied. Dislocations within the right slip band are visible using zone axis [1 1 2] and g = $(\bar{1}\,3\,\bar{1})$ (Fig. 12 a)), g = $(\bar{2}\,2\,0)$ (Fig. 12 b)) g = $(\bar{3}\,1\,1)$ (Fig. 12 c)) as well as zone axis [0 1 1] with g = $(\bar{3}\,1\,\bar{1})$ (Fig. 12 d)), whereas these dislocations are invisible under the combinations of zone axis [1 1 1] with g = $(2\,2\,\bar{4})$ (Fig. 12 e)) and zone axis [0 1 1] with g = $(\bar{2}\,\bar{2}\,2)$ (Fig. 12 f)).

According to the visibility/invisibility of dislocations under different two-beam conditions owing to the corresponding lattice strain, the Burgers vector of this set of dislocations can be determined and it is $[1\,\bar{1}\,0]$, which lies on the $(1\,1\,\bar{1})$ and $(1\,1\,1)$ planes. However, dislocations with Burgers vector of $[1\,\bar{1}\,0]$ can also slip on the $(1\,1\,2)$ plane. It is therefore not possible to distinguish between {1 1 1} and {1 1 2} planes for the underlying slip planes from this analysis.

Besides the high dislocation density and the associated dislocations in the slip bands, small straight lines that may be related to stacking faults have also been observed (indicated by arrows in Fig. 13). One set of these straight lines were found to lie predominantly on the $\left(11\,\bar{1}\right)$ plane, which are marked by a yellow arrow in Fig. 13. For the other stacking faults the corresponding planes could not be identified. The presence of stacking faults indicates that dislocations dissociate into partials leading misfits in stacking

Table 1
Micropillars 1–15 including their compression axes, the observed slip systems, Schmid factors (m_s), yield stresses (σ_y), and CRSS values.

Pillar	Pillar axis	Slip System	m_s	σ_y [GPa]	CRSS [GPa]
1	(1 7 10)	$(\bar{1}\,1\,\bar{2})[\bar{1}\,\bar{1}\,0]$	0.32	3.05	0.98
2		$(\bar{1}\,\bar{1}\,\bar{2})[\bar{1}\,10]$	0.34	2.67	0.94
3	$(\bar{9}\,1\,11)$	$(\bar{1}\,\bar{1}\,\bar{1})[110]$	0.33	3.37	1.11
4–6	$(1\,\bar{5}\,9)$	$(11\bar{1})[\bar{1}\,10]$	0.30	3.34	1.02
				3.13	0.94
				3.22	0.97
7 + 8	$(6\,\bar{1}3\,21)$	$(11\bar{1})[\bar{1}\,10]$	0.35	2.67	0.93
				3.05	1.07
9	$(13\,\bar{7}\,21)$	$(\bar{1}\,1\,\bar{1})[0\,\bar{1}\,1]$	0.36	2.43	0.87
10		$(11\bar{1})[\bar{1}\,0\,\bar{1}]$	0.30	2.25	0.98
11				2.24	0.97
12–14	$(12\,\bar{1}5\,7)$	$(111)[0\,\bar{1}\,1]$	0.26	3.88	1.01
		$(\bar{1}21)[\bar{1}\,0\,\bar{1}](11\bar{2})[\bar{1}\,10]$	0.46 0.31	3.56	* (1.64/1.10)
		$(\bar{1}21)[\bar{1}\,0\,\bar{1}](11\bar{2})[\bar{1}\,10]$	0.46 0.31	3.69	* (1.70/1.14)
15	$(\bar{7}\,1\,\bar{1}4)$	$(\bar{1}\,\bar{1}\,2)[1\,\bar{1}\,0]$	0.32	3.11	1.00

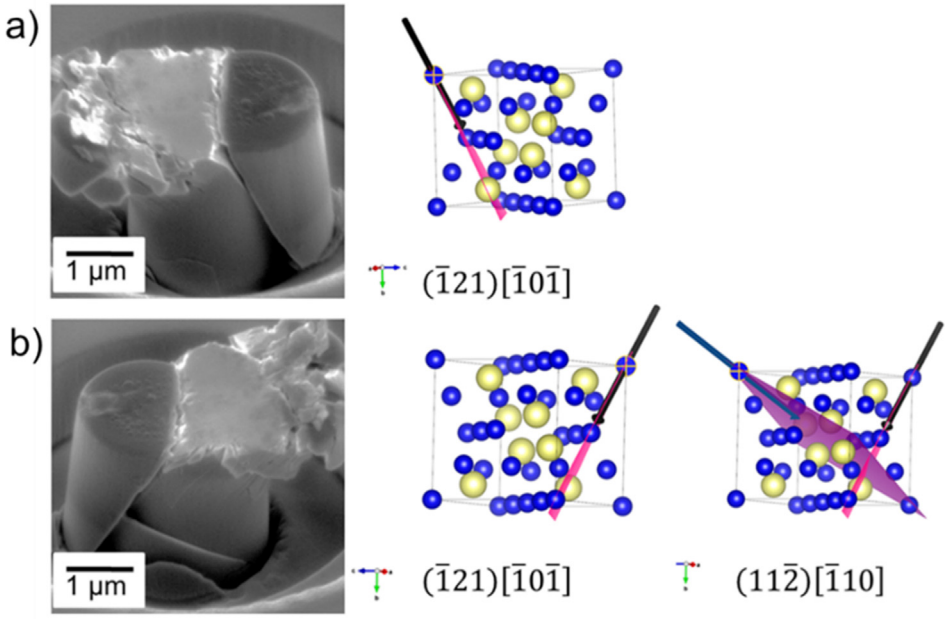

Fig. 9. SE-images of pillar 13 after deformation in a) front view including the corresponding unit cell and b) back view including the corresponding unit cell using VESTA [52].

Table 2
Presenting all nanomechanical measured properties of the $CaAl_2$ Laves phase.

Mechanical properties	Measured values
Hardness CSM	4.9 ± 0.7 GPa
Indentation Modulus	85.5 ± 4.0 GPa
Hardness SRJT	5.8 ± 0.8 GPa
Strain rate sensitivity	0.028 ± 0.019
Activation volume	0.530 ± 0.780 nm^3 3.75 ± 1.15 b^3
CRSS $\{111\}\frac{1}{2}\langle 1\bar{1}0\rangle$	2.96 ± 0.54 GPa
CRSS $\{112\}\frac{1}{2}\langle 1\bar{1}0\rangle$	2.94 ± 0.24 GPa

after their motion. Moreover, the occurrence of stacking faults on one of the triple layers is often correlated with the synchroshear process, which is thought to take place on the {1 1 1} planes.

4. Discussion

4.1. Mechanical properties

The measured hardness and indentation modulus at an indentation depth of 500 nm were consistent over all 10 different crystallographic orientations with a value of 4.9 ± 0.7 GPa and 85.5 ± 4.0 GPa. A recent study by Lou et al. [53] on $CaAl_2$ particles in a magnesium matrix revealed a hardness of 5.7 ± 0.4 GPa and an average Young's modulus of 82.9 ± 1.0 GPa, in good agreement with the values measured in the present study. The measured Young's modulus is also in good agreement with measurements on macroscopic single crystals by Schiltz and Smith [54], who measured elastic constants corresponding to a polycrystalline Young's modulus of 98 GPa, very close also to that predicted by ab initio calculations by Yu et al. [55], with an expected Young's modulus

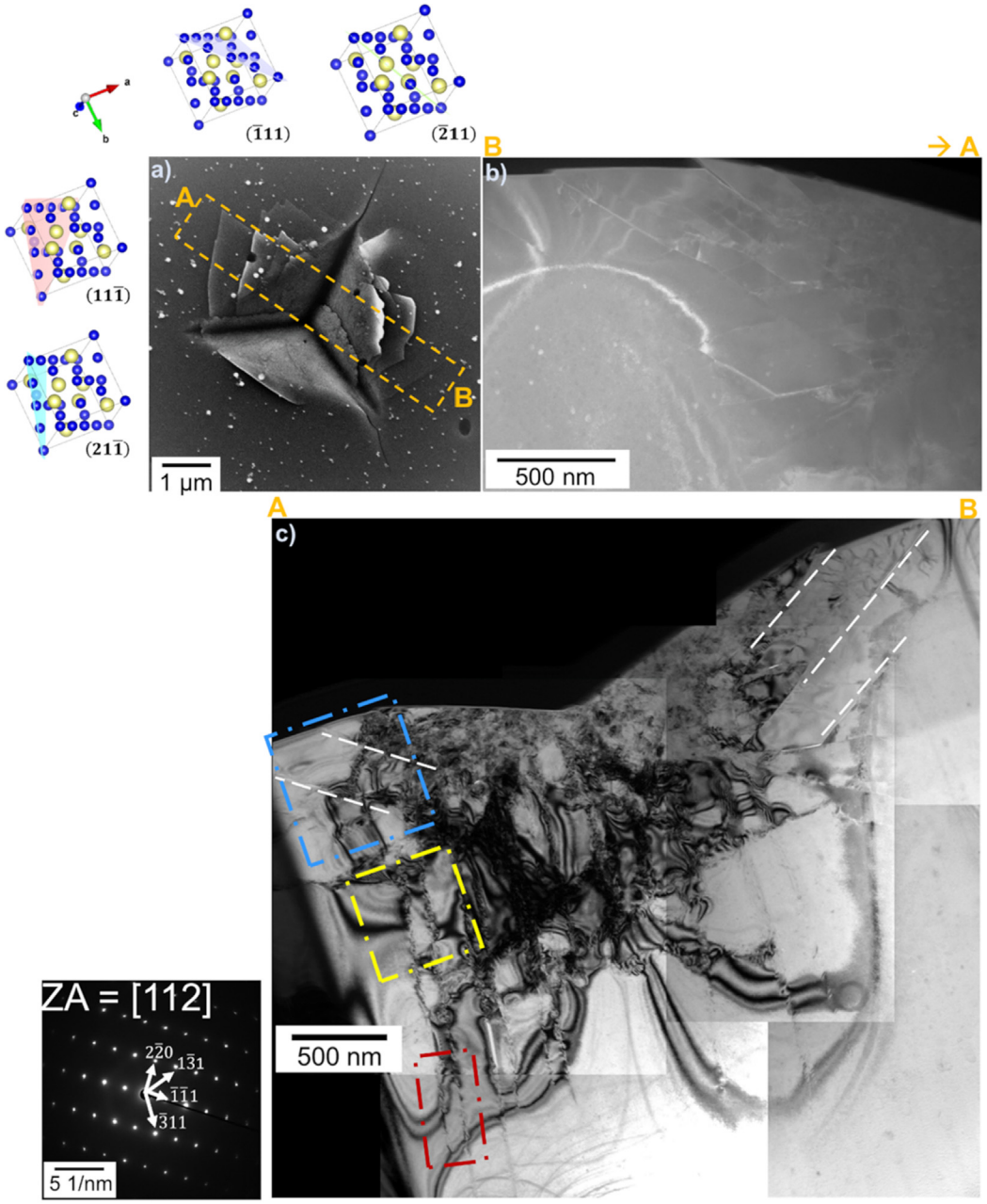

Fig. 10. A) se-image of a nanoindent including a schematic sketch (dotted orange area), from where the tem lamella was cut out. letters a and b show the orientation of the membrane and how it was analysed in the further investigations. the slip traces in the vicinity of the indent were furthermore correlated with different planes along with the unit cell using vesta[52]. b) STEM image of the lamella. c) BF-TEM image taken at [1 1 2] zone axis. The blue rectangle highlights the area with a high dislocation density (Fig. 11), whereas the red rectangle indicates the area where dislocation Burgers vector analysis was performed (Fig. 12) and the yellow rectangle corresponds to the area where the stacking faults from Fig. 13 were found. (For interpretation of the references to colour in this figure legend, the reader is referred to the web version of this article.)

at 0 K of 92 GPa. Measurements of the microhardness by Rokhlin et al. [12] for different holding periods (30 s and 3600 s) at 20 °C, resulting in 402 HV for 30 s and 354 HV for 3600 s, show the presence of creep for this duration and pressure. However, hardness values from macroscopic hardness measurements can be converted into values comparable to nanohardness using the equation from Fischer-Cripps [56,57] where hardness values from Vickers tests (HV) can be calculated in nanomechanical hardness (HN) by using the linear fit: $HV = 94.5 \cdot HN$, resulting in 3.94 GPa and 3.49 GPa respectively. These values are consistent with the calculated macroscopic hardness from our data using the Nix-Gao model, giving a value of 3.46 GPa [58].

Single crystal measurements of the elastic constants of $CaAl_2$ [54] gave a consistent absence of directional variation with an anisotropy factor of 0.98, i.e. very close to 1. Investigations of the hardness dependence on the crystal orientation for the $NbCo_2$ C15 Laves phase were performed by Luo et al. [26]. They investigated the hardness dependence on the orientation and stoichiometry applying nanoindentation tests on a diffusion couple and found that the hardness and the indentation modulus were unaffected by a change in orientation, which is consistent with the findings obtained here. Similar results were obtained by Zehnder et al. [40] for the hardness and indentation modulus of the hexagonal C14 $MgCa_2$ Laves phase after nanoindentation tests in different ori-

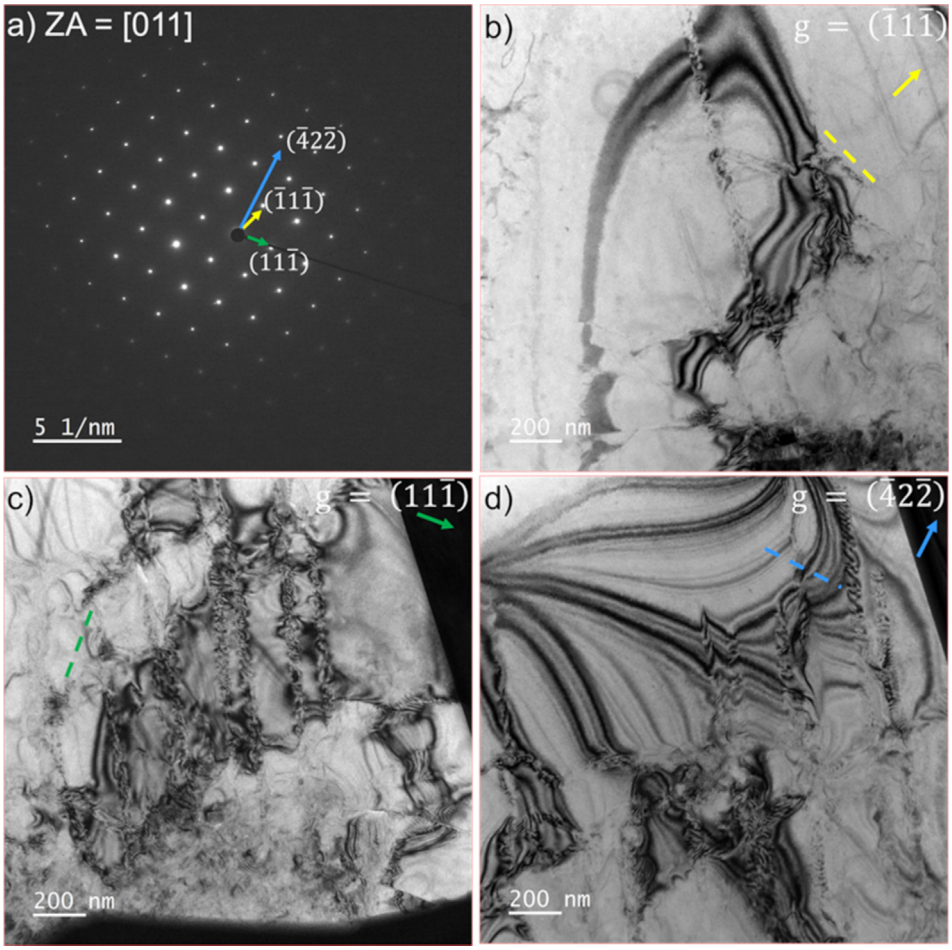

Fig. 11. TEM BF images showing dislocation substructure under the nanoindent (Fig. 10 a)) under 3 two-beam conditions with the same zone axis (a)). b) shows slip bands g = $(1\,1\,\bar{1})$, the yellow dashed line shows the alignment of the $(1\,1\,\bar{1})$ slip plane. c) displays the dislocation structure with g = $(1\,1\,\bar{1})$, the green dashed line symbolises the $(1\,1\,1)$ plane trace and in d) with g = $(4\,2\,\bar{2})$ the dislocations on the $(2\,1\,\bar{1})$ plane (blue dashed line) are shown. These images were taken in TEM with a 180° rotation of the lamella shown in Fig. 10. (For interpretation of the references to colour in this figure legend, the reader is referred to the web version of this article.)

entations, showing a constant hardness and indentation modulus for all measured orientations.

To compare the mechanical properties with the measured mechanical properties of Laves phases from previous room temperature deformation studies, the normalised CRSS will be determined by dividing the CRSS by the shear modulus. To compare these values, calculations were done analysing deformation along the planes containing the triple layer, i.e. for the C15 structure the (1 1 1) plane and for the C14 Laves phase the (0001) plane. For the $CaAl_2$ C15 Laves phase investigated in this study, a CRSS/G = 0.027 (with G ≈ 36 GPa) ratio was obtained. For the cubic $NbCo_2$ Laves phase, the normalized CRSS can be calculated to lie between 0.027 and 0.033 [28,29], while for the C14 Laves phase of the Mg-Al-Ca alloy it comes up to 0.023 at ambient temperature [40]. For the hexagonal $NbCo_2$ phase it results in 0.023, respectively, taking the results by Luo et al. [29]. As the available data below the BDTT is largely restricted to room temperature, with the exception of the lowest melting phase, which was also tested at elevated temperature [40], this comparison is necessary for slightly varying homologous temperatures. However, the melting points of the C15 and C14 phases in the Nb-Co system are very close. The finding that all values lie in the same range, while a trend to higher values can be observed for the cubic phases when comparing both structures.

Whether this is in fact the case or a result of a variation in shear modulus on the active slip plane compared to the isotropic shear modulus [59], could be investigated further by dedicated ab initio calculations of the triple layer slabs' stiffness and experiments at identical homologous temperatures on single crystalline micropillars oriented for slip on the {1 1 1} and {0001} planes.

4.2. Active slip systems

The statistical evaluation of the activated slip planes in the vicinity of the nanoindents (Fig. 6) revealed the activation of four different slip planes. The predominant slip plane was found to be the {1 1 1} plane (58.1 %), which is consistent with a previous publication by Paufler et al. [1] and studies [16,18,19] on the cubic $MgCu_2$ phase at elevated temperatures. However, the activation of the {1 1 2} plane was observed with a frequency of 47.5 %, which is only 10.6 % less often than the {1 1 1} plane.

There are several things to consider in interpreting this data, most importantly, the chance of double assignment of a slip trace where the traces of two (or more) planes are identical or very close to one another. The cubic system exhibits a total of four {1 1 1} planes but 12 {1 1 2} planes. This leads to a higher number of unambiguously identifiable {1 1 2} planes than {1 1 1} planes. Therefore, the expectation that those traces counted as a {1 1 2} trace, a greater fraction is in fact uniquely assigned, while many more {1 1 1} assignments also correspond to a possible {1 1 2} plane. A total number of 625 surface traces were correlated with plastic deformation, whereby the total amount of plane traces

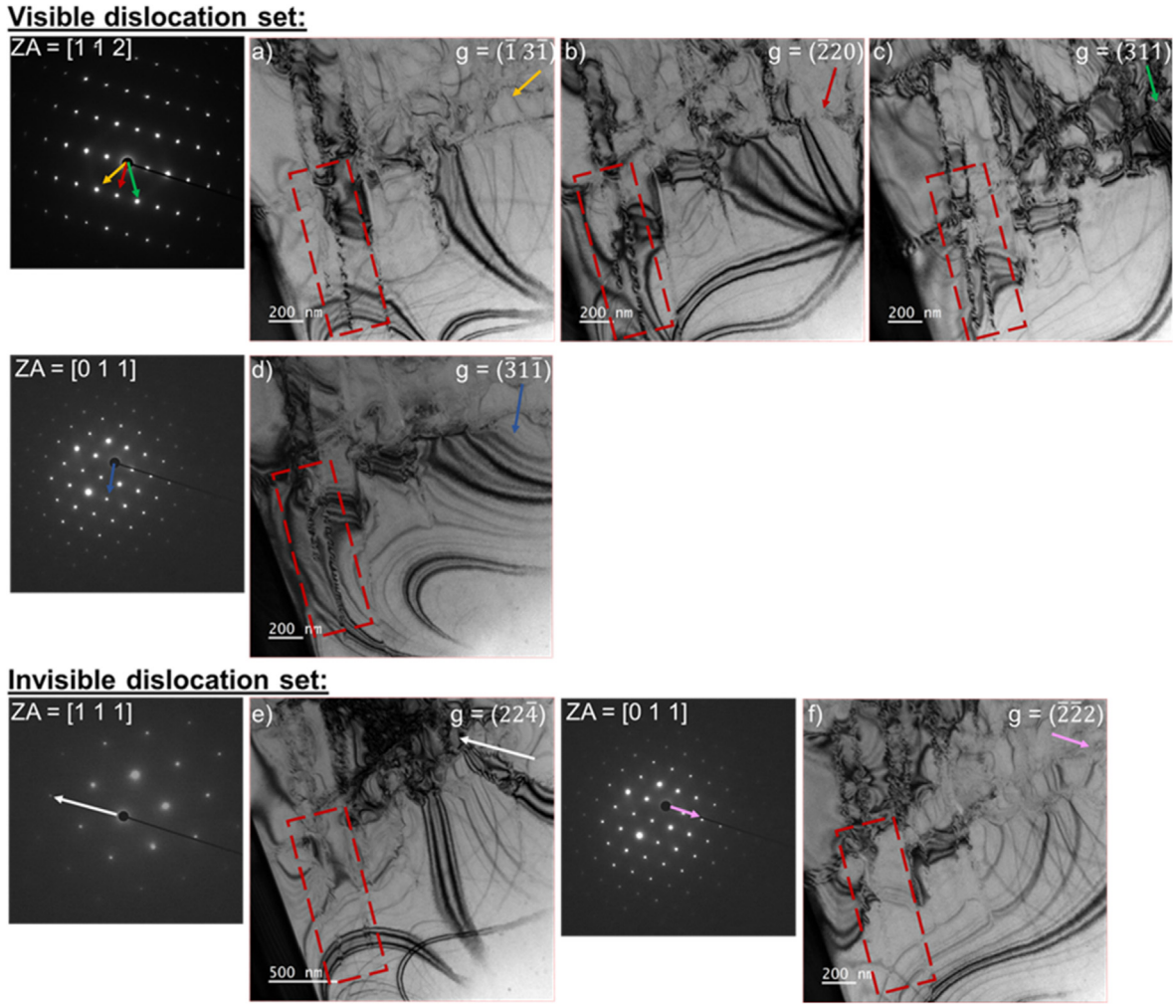

Fig. 12. TEM BF images showing dislocation substructure under the nanoindent (Fig. 10 a)) under different two-beam conditions. The red rectangle indicates the slip band, where the dislocation Burgers vector was analysed. The dislocation set is visible under a) g = (1 3 $\bar{1}$), b) g = ($\bar{2}$ 2 0) and c) g = ($\bar{3}$ 1 1) in [1 1 2] zone axis and under d) g = (3 1 $\bar{1}$) in [0 0 1] zone axis. They become invisible under e) g = (2 2 $\bar{4}$) in [1 1 1] zone axis and f) g = (2 $\bar{2}$ 2) in [0 1 1] zone axis. (For interpretation of the references to colour in this figure legend, the reader is referred to the web version of this article.)

was summed up to 811, because of double counting for those planes for which the deviation angle was below 3°. 23 % of the surface traces were counted twice. The double counted slip planes can be divided in 54 % (101 surface traces) for the {1 1 1} planes and 46 % (85 surface traces) for the {1 1 2} planes. With this knowledge about both corresponding to more or less the same number of double counting events, a purely geometrical artefact giving rise to the previously unexpected {1 1 2} slip plane can be excluded, because without double counting 212 surface traces were assigned to the {1 1 2} planes.

Now, a more detailed consideration of the geometry of the crystal and surface slip trace analysis, with its inherent double counting for planes yielding the same surface intersection or trace will follow. Given the higher probability of double counting for each of the 12 {1 1 2} planes compared to the 4 {1 1 1} planes, one might expect that for an equal division of unique slip traces, the {1 1 1} plane is softer, as it should otherwise only show a third of the number of traces. However, due to the different inclination of the two planes, there is also a difference in their likelihood of activation. While each of the 4 {1 1 1} planes possesses 3 independent Burgers vectors, giving a total of 12 independent slip systems, each of the 12 {1 1 2} planes contains only one possible Burgers vector, so that for a given identifiable plane, the {1 1 1} has a three times higher probability of having a favourably aligned Burgers vector giving a slip system with a high resolved shear stress. Overall, it would therefore appear that the slip trace analysis suggests no real difference in activation of the two slip systems on either {1 1 1} or {1 1 2} planes. This is in fact consistent with the observation from micro-compression that there is no significant difference in CRSS between the two systems for slip on either {1 1 1} or {1 1 2} planes.

Since it is not possible to unambiguously identify the Burgers vector from micropillar compression experiments, although it is needed to estimate a critical resolved shear stress, TEM investigations were performed on nanoindents with their greater variety of active slip planes and greater gradient in dislocation density enabling a better selection of conditions for dislocation strain field imaging towards the edge of a plastic zone. By conducting a $g \cdot b$ extinction analysis, the Burgers vector could be identified as $<10\bar{1}>$, which is contained in both identified slip planes. Furthermore, besides perfect dislocations, the presence of stacking faults, especially on a {1 1 1} planes, points towards the motion of at least partly dissociated dislocations by the well-known synchroshear mechanism in the triple layer [30–33].

The CRSS for plastic deformation on both slip systems in micro-compression was then found to be 0.99 ± 0.03 GPa for {1 1 1} $<1\bar{1}0>$ and 0.97 ± 0.07 GPa for {1 1 2}$<1\bar{1}0>$. There are no other studies on round micropillars from bulk $CaAl_2$ for a direct quanti-

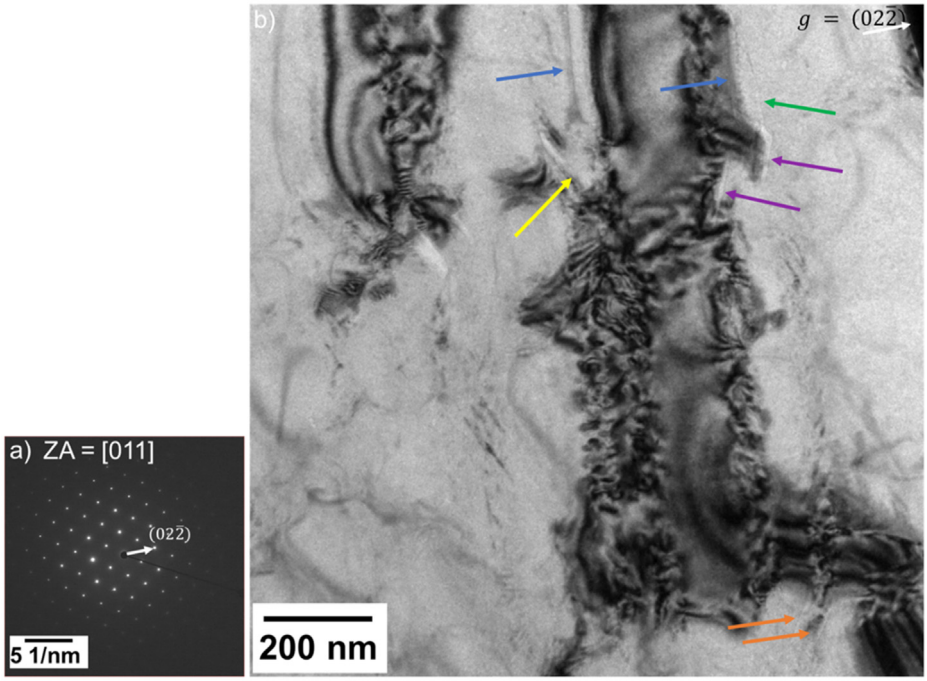

Fig. 13. Higher magnification TEM BF image showing the area marked by the yellow rectangle in Fig. 10. This image was taken under g vector (02$\bar{2}$) in [011] zone axis. Stacking faults with different orientations are indicated by arrows with different colours. The yellow ones show stacking faults parallel to the (111) plane trace. (For interpretation of the references to colour in this figure legend, the reader is referred to the web version of this article.)

tative comparison with our data, but agreement can be found with respect to the work on square pillars in $CaAl_2$ precipitates, since this work must also take into account the effects of stoichiometry on the plasticity of the Laves phase, which are largely unknown.

A previous study by Luo et al. [53] also reported the {111} <1$\bar{1}$0> slip system in $CaAl_2$ precipitates to represent the major slip system after performing micropillar compression tests at ambient temperature. Their measured CRSS value was 164.9 MPa, which is a factor of 6 lower than measured in our experiments. However, considering that their micropillars had a square cross-section of 4 μm × 4 μm compared to our round micropillar with a diameter of 2.1 μm, the deviation might in part originate from the size effect on dislocation motion and easier dislocation nucleation at the edges of square pillars, giving a smaller contribution from nucleation to the overall stress level and a potentially higher dislocation density, which would lead to a reduction in CRSS in a lattice resistance controlled material. A micropillar study using round and square micropillars [60,61] showed that for both types, mechanisms of collective cross-slip were observed between two planes of the same plane family and with the same high Schmid factor, whereas the measured initial stress was greater for the round geometry. From the Laue analysis and post mortem SEM, the deformation zone of the square micropillar was found to be more pronounced and showed different activated slip systems.

In addition, a deviation from the stoichiometric composition may influence the mechanical properties [53], because the C15 Laves phase particles, embedded in a Mg matrix phase, compressed by Luo et al. showed a deviation of ~ 5.7 at.-% for Al and ~ 2.0 at.-% for Ca from the ideal composition. However, it is still not clear how a deviation from the ideal stoichiometry influences the mechanical properties and therefore how to estimate an expected change in CRSS with composition. Some studies [1,62,63] suggest a decreasing hardness for a deviation from the ideal composition, whereas another study [26] reported an increase of the hardness.

On a qualitative level, our detection of {111}<1$\bar{1}$0> slip is very typical for C15 Laves phases at room temperature and in good agreement with previous studies by Luo et al. for $CaAl_2$ [53], Xue et al. [27] for the $CrNb_2$ phase, Luo et al. [29] and Korte et al. [28].

On the other hand, deformation on the {112} plane has not yet been reported for intermetallic phases of C15 type at room temperature so far, to the authors' best knowledge. However, the high frequency and often unique assignment of slip traces to {112}, its identification by TEM and on the surface of micropillars, prove the occurrence of slip on {112} planes.

Preferential deformation was expected along the triple layer, which lies along the {111} planes in the C15 structure, but deformation on non-basal planes, away from the triple layer (along {0001} planes), has in fact previously been described for hexagonal Laves phases with the C14 structure in several studies at ambient and elevated temperature [40,41]. Additionally, micropillar compression tests of the $CaMg_2$ C14 Laves phase at room temperature have revealed that the CRSS is comparatively low for the 1st order prismatic slip system [27,40].

For a comprehensive comparison, the CaMg2 Laves phase was chosen because of its similar structure and also the presence of similar elements on the A site of the AB2 Laves phase structure. Additionally, for this phase more data are available in the literature including the slip line activation on different planes and CRSS values.

For the evaluation of the {112} slip system, a comparison of the analysed structure of the cubic C15 and the hexagonal C14 Laves phases was done. It could be observed that a similar stacking to the cubic {112} plane can be found in the hexagonal structure and can be related to previously reported non-basal slip plane. In Fig. 14 both structures are displayed. The black line shows the plane along the triple layer (in C15 the (111) and C14 the (0001) plane) for both packings. The position of three parallel (112) planes is shown for the cubic C15 Laves phase with pink lines. A comparatively similar stacking sequence is in fact found along the {10$\bar{1}$0} plane (1st order prismatic plane) of the hexagonal C14 Laves phase (Fig. 14 pink line). Both reveal a triple stacking with an A-B-A (Ca-Al-Ca or Ca-Mg-Ca) stacking. For the C14 struc-

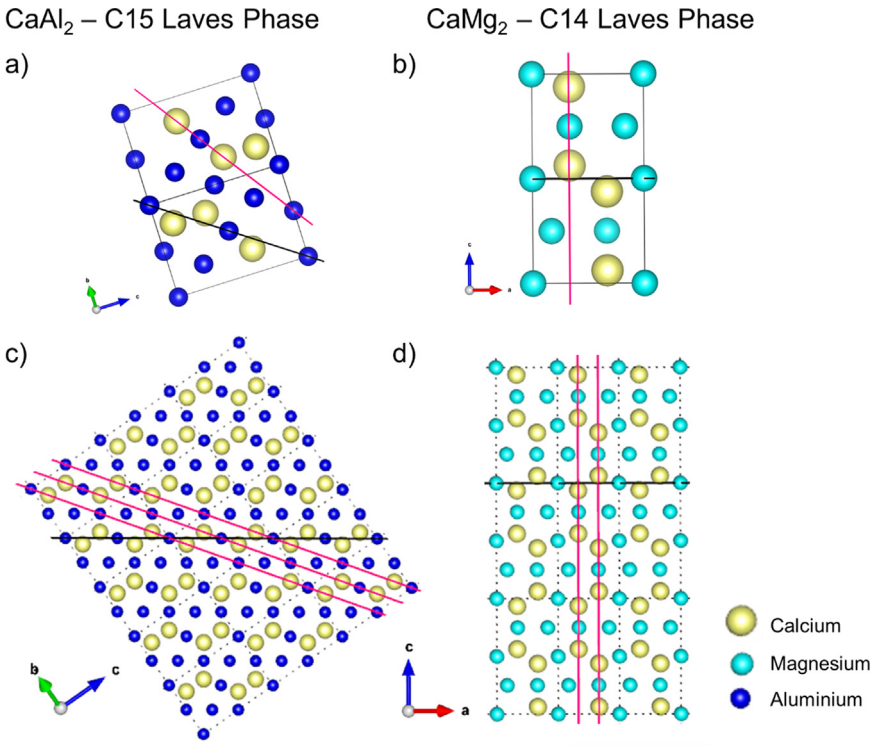

Fig. 14. Visualisation of the (1 1 1) plane (black line) and (1 1 2) plane (purple line) in the $CaAl_2$ phase and the (0001) plane (black line) and the $(10\bar{1}0)$ plane (purple line) in the $CaMg_2$ phase by using VESTA, whereby a) and b) displays the different unit cells aligned for a crystallographic comparison for the planes [52]. (For interpretation of the references to colour in this figure legend, the reader is referred to the web version of this article.)

ture these repeat continuously along the prismatic plane, while for the C15 structure the Kagomé layer is intersected, placing the repeating unit at some distance and with an Al atom in between. Considering that the prismatic plane is the easiest slip plane in the $CaMg_2$ C14 phase, deformation by a similar mechanism on the {1 1 2} plane in C15 does not appear too unreasonable. The effect of the disturbed repeat unit along the plane on dislocation glide cannot be readily anticipated as so little is known about glide on this type of plane. The curved slip lines found frequently at the indents might be indicative of high cross-slip activity. Cross slip might be a preferential slip mode due to a reduced confinement of dislocations to a specific set of parallel {1 1 2} planes and a tendency to follow the repeating motif to make the glide path more similar to the prismatic plane in the C14 phase.

In addition to considering the qualitative possibility of slip on the {1 1 2} planes, the expected quantitative values for the CRSS can also be compared, at least relatively speaking, based on the interplanar spacing of the slip plane, which strongly affects the dislocation width and consequently Peierls stress for a given Burgers vector [64]. For the triple layer, the $CaAl_2$ phase reveals a closer interplanar spacing. These values are listed in Table 3 compared with the $CaMg_2$ phase. The interplanar spacings of both (ideal) structures are caused by the different constituent atoms and their atomic radii. Ca possesses the largest radius with 197 pm, followed by Mg with 160 pm and Al with 143 pm [65,66]. This leads to the closer interplanar spacing in the triple sequence of the (1 1 2) plane in $AlCa_2$ than for the $(10\bar{1}0)$ plane in $CaMg_2$. The difference between these distances amounts to 0.32 Å. The continuously repeating triple sequence of the $(10\bar{1}0)$ plane in $CaMg_2$ has a smaller interplanar spacing than the distance between the triple sequence and the intersecting Al atom from the Kagomé layer of the (1 1 2) plane in $CaAl_2$. Additionally, the arrangement of the parallel {1 1 2} planes repeats continuously, revealing a small overlap

Table 3
Interplanar spacing of the triple layers and the (1 1 2) and $(10\bar{1}0)$ planes. The distances were measured along the plane from the center of one atom to the other.

$CaAl_2$	spacing	$CaMg_2$	spacing
(1 1 1)		**(0001)**	
Al ↔ Ca	3.33 Å	Mg ↔ Ca	3.65 Å
Ca ↔ Ca	3.47 Å	Ca ↔ Ca	3.82 Å
Ca ↔ Al	3.33 Å	Ca ↔ Mg	3.65 Å
(1 1 2)		$(10\bar{1}0)$	
Ca ↔ Al ↔ Ca (spacing in triple sequence)	3.33 Å	Ca ↔ Mg ↔ Ca (spacing in triple sequence)	3.65 Å
Al ↔ triple sequence ↔ Al	7.70 Å	Between triple sequences	6.37 Å
Lattice distance	1.64 Å	Lattice distance	1.78 Å

from the triple layer on one plane to the triple layer on the next parallel plane with a lattice distance of 1.64 Å (distance between the purple lines displaced in Fig. 14). Looking at the alignment of the $(10\bar{1}0)$ plane, there are only two parallel layers, with a lattice spacing of 1.78 Å, which also is smaller than the full distance to the next triple layer in the plane.

With the comparison of these planes and the knowledge of the low CRSS for 1st order prismatic slip systems in C14 Laves phases, the possibility of the activation of {1 1 2} slip cannot be entirely explained or connected with a distinct dislocation mechanism, but its occurrence can be rationalised from this comparison.

4.3. Active fracture planes

In contrast, the nucleated cracks could clearly be measured to be the {1 1 2} plane. The identification of the crack planes is clearer than that of the slip lines due to smaller encountered overlaps in these cases for the {1 1 1} and {1 1 2} planes compared to the slip line analysis. The TEM analysis (Fig. 10) further revealed planar

cracks within the volume and along slip traces extending from the volume to the surface on the $(2\bar{1}1)$ and $(21\bar{1})$ planes. During indentation, the applied pressure would provide a driving force for these cracks to open. Therefore, this leads to the assume that plasticity occurred first on these planes and that upon unloading, the accumulation of dislocation defects further promoted decohesion along these apparently favourable {112} fracture planes. A very similar observation has been made by Schröders et al. [51] during indentation and microcompression of the structurally related μ-phase and crack nucleation at intersecting slip bands in general is a commonly observed phenomenon at large and small scales [25,67,68].

4.4. Orientation dependence of slip morphology

Beside the straight lines and edges, which could be used to clearly identify active slip systems that were confirmed in both microcompression and TEM, curved traces were also detected around the indents (Fig. 5), which could not be assigned to individual underlying slip planes. This occurrence of both curved and straight slip traces is similar to what was observed by the authors in deformation of the $CaMg_2$ C14 Laves phase at elevated temperatures [41] and also for the Fe_7Mo_6 μ-phase at ambient temperature [51], but could not yet be assigned to a specific deformation mechanism beyond speculation that possible reasons may be easy cross-slip or promotion of cross-slip where slip systems interact.

One might expect these to result in an orientation dependence in terms of the prevalent slip morphology and this is indeed observed (Fig. 4). Grains near the [011] direction exhibit edged and straight lines around the deformation zone, while grain orientations near [111] only reveal cracks. For orientations near [001] direction straight lines and further curved deformation can be seen. The orientations between these three directions in the centre of the standard triangle exhibit all deformation morphologies concurrently.

This can be rationalise as follows:

For deformation with the major stress along [111] (either as a close approximation in microcompression of a (111) oriented crystal or a rough approximation for indentation on the same surface plane), there is no {111} plane with a non-zero Schmid factor as all planes are either perpendicular to the surface or the Burgers vector within the surface plane. In case of the {112} planes, there are three sets of planes, those lying perpendicular to the surface (one indicated in yellow in Fig. 15), those with the Burgers vector in the surface plane (red in Fig. 15) and those inclined to the surface at a shallow angle and the Burgers vector also out of the surface plane (grey and violet in Fig. 15). Only the latter achieve a non-zero Schmid factor. While the first can leave no slip trace, the second would be more likely to crack for a favourable fracture plane and the last are at the very least unlikely to form slip traces unless slip can very easily expand outwards from the highest pressure zone to intersect the surface at some horizontal distance away. For the two identified slip system families and the {112} a favourable crack plane, the observed cracks and an absence of slip traces is therefore consistent with expectations.

In [011] and [001] orientation, straight traces as well as edges (i.e. very short, connected segments of different orientations) or curves, respectively, occurred. This can also be rationalised based on the orientation of the available slip planes. Leaving again those unconsidered which are unlikely to form slip traces (those {211} planes with a shallow inclination to a {011} surface plane or those (nearly) normal to the surface, which would rather serve as fracture planes), suitable slip planes with intermediate Schmid factors can be found for both the {111} and {211} planes. However, while in case of a {011} surface these form a twofold symmetry with an orientation spread from 4 potential slip planes (a central {111} and 3 {211}) each, in case of a {001} surface these are grouped around the 4 {111} poles to give a much more continuous orientation spread. The observation of the more ragged edges in case of the first case of a {011} surface and more continuously curved traces in case of the {001} surface is therefore equally consistent with deformation on the two slip plane families and cross-slip occurring between them owing to the shared Burgers vector.

Finally, further away from the low index axis orientations, where both slip systems have systems with high Schmid factors (Fig. 4) and many differently oriented planes, a mixture of these regimes is expected and observed.

In addition to dislocation slip, twinning was mostly reported as occurring deformation mechanism at room temperature for cubic Laves phases in macroscopic studies [12,13], but was not observed in our study doing micropillar compression tests or in the analysed TEM lamella.

4.5. Activation volume

Strain rate jump tests revealed a strain rate sensitivity of 0.028 ± 0.019 for the C15 phase and an overall average activation volume of 3.75 ± 1.15 b^3, for a Burgers vector along the closed packed direction $\frac{a}{2}\langle 110\rangle$ (b = 0.5685 nm). Due to the close packed structure of the Laves phases, the intrinsic resistance against plastic deformation is assumed to be comparatively high, especially compared to metals with a simple face centred cubic structure. Additionally, the fact of having a BDTT shows the strong influence of thermal activation for plasticity, and therefore the activation volume should be comparatively low, as measured in the strain rate jump test. An activation volume around $\sim 10\ b^3$ is usually correlated with the mechanisms of overcoming the Peierls barrier, giving rise to the lattice resistance, by forming and moving kink pairs, in contrast to overcoming a field of discrete obstacles like other dislocations or precipitates [70]. However, other mechanisms are associated with similar activation volumes, particularly cross-slip and climb. Both are difficult to be observed directly by TEM, but at least climb, which is based on the diffusion of vacancies to dislocations, may be considered unlikely here as experiments were carried out at low homologous temperatures, where diffusional processes of flow are not usually dominant. In contrast, dislocation motion affected by solute drag and the diffusion speed of the solutes in comparison to the dislocation velocity, is known to lead to strong experimental signatures in the form of serrated flow.

Serrations have been reported in the loading curves for different intermetallic phases like the hexagonal $CaMg_2$ as well as for the cubic $Mg_{17}Al_{12}$ for nanoindentation tests at room temperature or 50 °C, decreasing with increasing temperature [11,41]. The room temperature activation volume for the γ-$Mg_{17}Al_{12}$ phase was estimated as 4.8 b^3 by Mathur et al. [11], however, the authors could also not unambiguously assign this volume to either dislocation motion controlled by overcoming the Peierls barrier or solute drag effects.

In the literature on high temperature Laves phase deformation in bulk samples, in particular $MgZn_2$, attempts to provide deformation mechanism maps suffer from similar limitations [71]. Macroscopically, data on yield stresses is only available down to the BDTT at a homologous temperature of around 0.6. In the plastic regime (in compression) above this temperature and up to the point of the onset of dislocation climb at higher temperatures and low stresses, dislocation glide and climb are thought to be the governing mechanisms with glide assumed to be rate limiting [71]. Observations of yield drops support the assumption that such mechanisms with a strong inverse dependence of the stress on mobile dislocation density are operating [15,72]. However, the

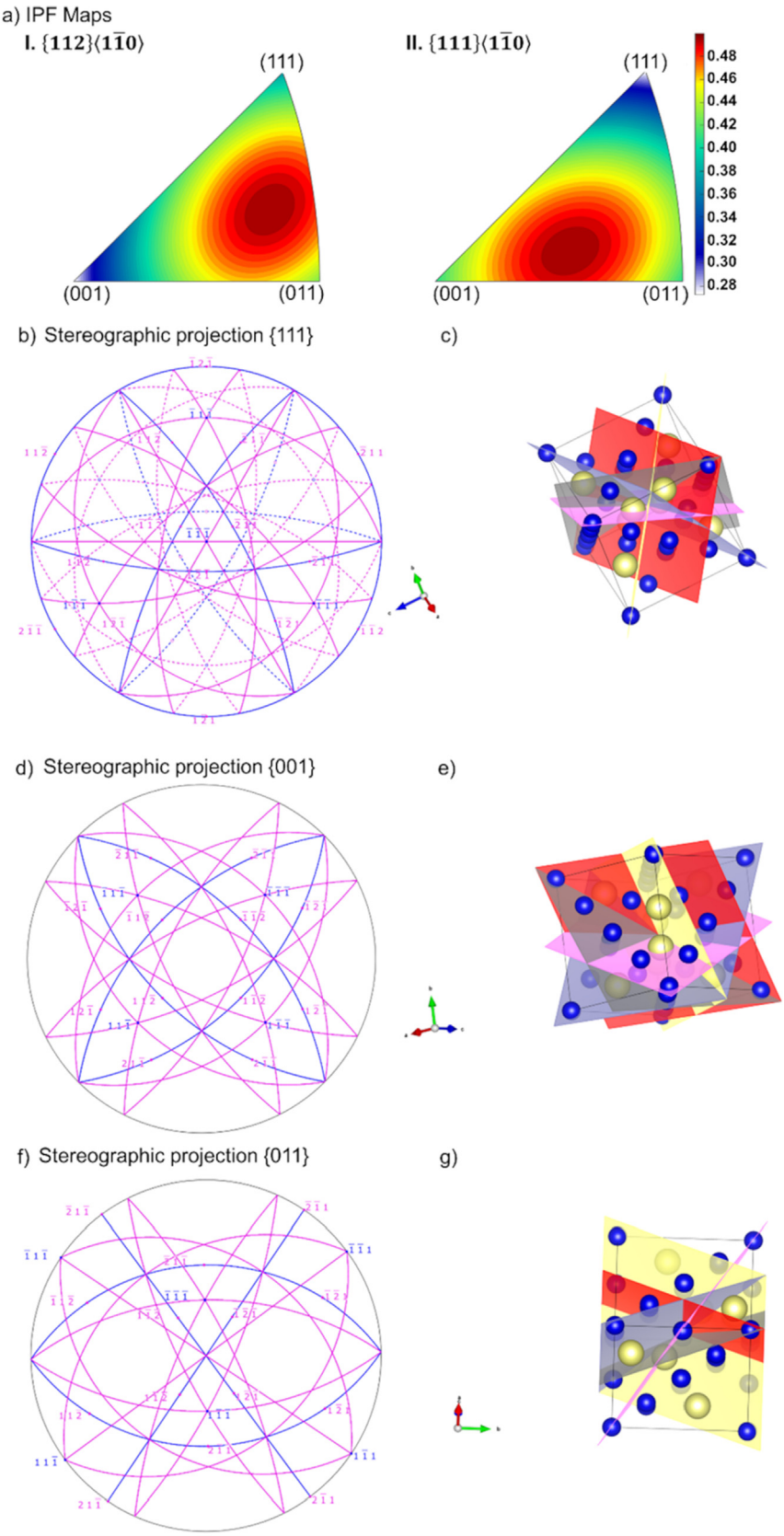

Fig. 15. A) displays the schmid factor distribution for i. {1 1 2}< 1 $\bar{1}$ 0 > and II. {1 1 1}< 1 $\bar{1}$ 0 > in an IPF map. In b), d), f) the stereographic projection of the b) {1 1 1}, d) {0 0 1} and f) {0 1 1} traces (in blue) with ⟨2 1 1⟩ poles (in pink) is shown using Crystal Maker [69]. c), e), g) visualises [52] the alignment of the {1 1 2} planes in the unit cells of the experimentally found orientations that were the closest to the c) {1 1 1}, e) {0 0 1} and g) {0 1 1} (surface) plane normal (here facing upwards). (For interpretation of the references to colour in this figure legend, the reader is referred to the web version of this article.)

observation of serrations and also immobilisation of dislocations in interrupted mechanical tests [15], also points to a further role of point defects in the deformation of Laves phase crystals. Given that off-stoichiometric composition has been found to lead to softening in many but not all cases, it can be concluded here that in the $CaAl_2$ C15 Laves phase it is likely that at low temperature the lattice resistance provides the rate limiting mechanism, but that cannot infer if or in how far this is also affected by solutes. Additionally, studies above the BDTT on cubic Laves phases calculated a decreasing strain rate sensitivity and the activation volume with increasing temperature and correlating it also with the overcoming of the Peierls barrier, which could also be correlated diffusion or climb processes at these experimental temperatures [73,74].

However, the work presented here and elsewhere on Laves phases in recent years now puts us into a position to investigate these effects in more detail and with hopefully more definite conclusions. With respect to the $CaAl_2$ phase, future work towards elevated temperatures and also towards off-stoichiometric or alloyed compositions can follow. Taking into account the new insights on the active dislocation slip systems and the dependence of likely cross-slip opportunities on crystal orientation in indentation presented above, the expectation that work at temperatures between room temperature and the BDTT as well as on alloys will be able to draw firmer conclusions on the individual roles of the lattice resistance on individual slip systems and solutes, anti-site defects or vacancies in governing dislocation motion in Laves phases. In experiments, the different point defects may not be possible to control separately, however, in simulations, first efforts are already being made to explore their role on dislocation motion [75].

5. Conclusions

The plasticity of the $CaAl_2$ C15 phase was investigated at ambient temperature using nanoindentation in conjunction with a slip trace analysis, strain rate jump tests, micropillar compression and TEM analysis. The combination of these testing methods allowed us to draw the following conclusions:

- The average hardness and indentation modulus are 4.9 ± 0.7 GPa and 85.5 ± 4.0 GPa and do not vary significantly with orientation.
- Strain rate jump tests reveal a strain rate sensitivity of 0.028 ± 0.019 and a corresponding activation volume of 3.75 ± 1.15 b^3.
- All nanomechanical experiments have shown that the predominate slip systems are $\{111\}\langle 1\bar{1}0\rangle$ and $\{112\}\langle 1\bar{1}0\rangle$ and are activated with more or less the same CRSS of 0.99 ± 0.07 GPa and 0.97 ± 0.03 GPa, respectively, whereby TEM investigations allowed to identify the $[1\bar{1}0]$ Burgers vector type by using the $g \cdot b$ analysis.
- Cracks at the edge of the indents were found on the {1 1 2} plane for all investigated orientations.
- TEM analysis on a nanoindent allowed to identify dislocation motion on both $(11\bar{1})$ and $(\bar{2}1\bar{1})$ planes. Stacking faults were found and could be located on the $(11\bar{1})$ plane.

Data availability

The authors do not have permission to share data.

Declaration of Competing Interest

The authors declare that they have no known competing financial interests or personal relationships that could have appeared to influence the work reported in this paper.

Acknowledgements

The authors gratefully acknowledge financial support by the Deutsche Forschungsgemeinschaft (DFG) to all projects involved in this paper A05, Z and S the SFB1394 Structural and Chemical Atomic Complexity – From Defect Phase Diagrams to Material Properties, project ID 409476157. This project has received funding from the European Research Council (ERC) under the European Union's Horizon 2020 research and innovation programme (grant agreement No. 852096 FunBlocks). H. Springer gratefully acknowledges funding through the Heisenberg program of the DFG (project number 416498847).

References

[1] P. Paufler, Early work on Laves phases in East Germany, Intermetallics 19 (4) (2011) 599–612.
[2] F. Stein, A. Leineweber, Laves phases: a review of their functional and structural applications and an improved fundamental understanding of stability and properties, J. Mater. Sci. 56 (9) (2021) 5321–5427.
[3] J. Livingston, Laves-phase superalloys?, Phys Status Solidi A 131 (2) (1992) 415–423.
[4] A.-P. Hynninen et al., Self-assembly route for photonic crystals with a bandgap in the visible region, Nat. Mater. 6 (3) (2007) 202–205.
[5] B. van der Meer et al., High antisite defect concentrations in hard-sphere colloidal laves phases, Soft Matter 16 (17) (2020) 4155–4161.
[6] B.A. Lindquist, R.B. Jadrich, T.M. Truskett, From Close-Packed to Topologically Close-Packed: Formation of Laves Phases in Moderately Polydisperse Hard-Sphere Mixtures. arXiv preprint arXiv:1803.03327, 2018.
[7] A. Suzuki et al., Structure and transition of eutectic (Mg, Al) 2Ca Laves phase in a die-cast Mg–Al–Ca base alloy, Scr. Mater. 51 (10) (2004) 1005–1010.
[8] H.A. Elamami et al., Phase selection and mechanical properties of permanent-mold cast Mg-Al-Ca-Mn alloys and the role of Ca/Al ratio, J. Alloy. Compd. 764 (2018) 216–225.
[9] M. Zubair et al., On the role of Laves phases on the mechanical properties of Mg-Al-Ca alloys, Mater. Sci. Eng. A 756 (2019) 272–283.
[10] D. Amberger, P. Eisenlohr, M. Göken, Microstructural evolution during creep of Ca-containing AZ91, Mater. Sci. Eng. A 510 (2009) 398–402.
[11] H. Mathur, V. Maier-Kiener, S. Korte-Kerzel, Deformation in the γ-$Mg_{17}Al_{12}$ phase at 25–278° C, Acta Mater. 113 (2016) 221–229.
[12] L. Rokhlin et al., Calcium-alloyed magnesium alloys, Met. Sci. Heat Treat. 51 (3–4) (2009) 164.
[13] T. Müller et al., Gleitbanduntersuchungen während und nach Verformung der intermetallischen Verbindung $MgZn_2$, Krist. Tech. 7 (11) (1972) 1249–1264.
[14] D. Hinz, P. Paufler, G. Schulze, Temperature change experiments during secondary creep of the intermetallic compound $MgZn_2$, physica status solidi (b) 36 (2) (1969) 609–615.
[15] T. Müllerr, P. Paufler, Yield strength of the monocrystalline intermetallic compound $MgZn_2$, physica status solidi (a) 40 (2) (1977) 471–477.
[16] U. Krämer, G. Schulze, Gittergeometrische Betrachtung der plastischen Verformung von Lavesphasen, Krist. Tech. 3 (3) (1968) 417–430.
[17] A. Von Keitz, G. Sauthoff, Laves phases for high temperatures—Part II: Stability and mechanical properties, Intermetallics 10 (5) (2002) 497–510.
[18] P. Paufler, G. Schulze, Gleitsysteme innermetallischer Verbindungen, Krist. Tech. 2 (4) (1967) K11–K14.
[19] J. Moran, Mechanical behavior of $MgCu_2$ single crystals, Trans. Metall. Soc. AIME 233 (8) (1965) 1473.
[20] D.P. Pope, F. Chu, Deformation of a C15 Laves phase: Twinning and synchroshear, Structural intermetallics (1993).
[21] W.-Y. Kim, D.E. Luzzi, D.P. Pope, Room temperature deformation behavior of the Hf–V–Ta C15 Laves phase, Intermetallics 11 (3) (2003) 257–267.
[22] A. Kazantzis, M. Aindow, I. Jones, Deformation behaviour of the C15 Laves phase Cr_2Nb, Mater. Sci. Eng. A 233 (1–2) (1997) 44–49.
[23] A. Kazantzis et al., The mechanical properties and the deformation microstructures of the C15 Laves phase Cr_2Nb at high temperatures, Acta Mater. 55 (6) (2007) 1873–1884.
[24] A. Kazantzis, M. Aindow, I. Jones, Stacking-fault energy in the C15 Laves phase Cr_2Nb, Philos. Mag. Lett. 74 (3) (1996) 129–136.
[25] S. Korte-Kerzel, Microcompression of brittle and anisotropic crystals: recent advances and current challenges in studying plasticity in hard materials, MRS Commun. 7 (2) (2017) 109–120.
[26] W. Luo et al., Composition dependence of hardness and elastic modulus of the cubic and hexagonal $NbCo_2$ Laves phase polytypes studied by nanoindentation, J. Mater. Res. 35 (2) (2020) 185–195.
[27] Y. Xue et al., Critical resolved shear stress of activated slips measured by micropillar compression tests for single-crystals of Cr-based Laves phases, Mater. Sci. Eng. A 806 (2021) 140861.
[28] S. Korte, W.J. Clegg, Studying plasticity in hard and soft Nb–Co intermetallics, Adv. Eng. Mater. 14 (11) (2012) 991–997.

[29] W. Luo et al., Crystal structure and composition dependence of mechanical properties of single-crystalline $NbCo_2$ Laves phase, Acta Mater. 184 (2020) 151–163.
[30] M.F. Chisholm, S. Kumar, P. Hazzledine, Dislocations in complex materials, Science 307 (5710) (2005) 701–703.
[31] Hazzledine, P., et al., *Synchroshear of Laves phases.* MRS Online Proceedings Library (OPL), 1992. **288**.
[32] P. Hazzledine, P. Pirouz, Synchroshear transformations in Laves phases, Scr. Metall. Mater. 28 (10) (1993) 1277–1282.
[33] J. Guénolé et al., Basal slip in Laves phases: the synchroshear dislocation, Scr. Mater. 166 (2019) 134–138.
[34] Z. Xie et al., Laves phase crystal analysis (LaCA): Atomistic identification of lattice defects in C14 and C15 topologically close-packed phases, J. Mater. Res. 36 (10) (2021) 2010–2024.
[35] S. Schröders et al., On the structure of defects in the Fe_7Mo_6 μ-Phase, Acta Mater. 167 (2019) 257–266.
[36] Y. Liu, J.D. Livingston, S.M. Allen, Defect structures and nonbasal slip of C36 laves phase $MgNi_2$ in a two-phase alloy, Metall. Mater. Trans. A 26 (6) (1995) 1441–1447.
[37] Liu, Y., S.M. Allen, and J.D. Livingston, *Deformation mechanisms in a Laves phase.* MRS Online Proceedings Library (OPL), 1992. **288**.
[38] Y. Liu, S.M. Allen, J.D. Livingston, Deformation of two C36 laves phases by microhardness indentation at room temperature, Metall. Mater. Trans. A 26 (5) (1995) 1107–1112.
[39] Allen, S., *Slip, twinning, and transformation in Laves phases.* , A.-.-J. Final technical report, 1997, Editor. 1998, Massachusetts Inst. of Technology (MIT), Cambridge, MA (United States).
[40] C. Zehnder et al., Plastic deformation of single crystalline C14 Mg_2Ca Laves phase at room temperature, Mater. Sci. Eng. A 759 (2019) 754–761.
[41] M. Freund et al., Plastic deformation of the $CaMg_2$ C14-Laves phase from 50–250° C, Materialia 20 (2021) 101237.
[42] D. Andre et al., Metallographic preparation methods for the Mg based system Mg-Al-Ca and its Laves phases, Mater Charact (2022) 112187.
[43] W.C. Oliver, G.M. Pharr, An improved technique for determining hardness and elastic modulus using load and displacement sensing indentation experiments, J. Mater. Res. 7 (6) (1992) 1564–1583.
[44] P.S. Phani, W. Oliver, A critical assessment of the effect of indentation spacing on the measurement of hardness and modulus using instrumented indentation testing, Mater. Des. 164 (2019) 107563.
[45] J.-S.-L. Gibson et al., Finding and Characterising Active Slip Systems: A Short Review and Tutorial with Automation Tools, Materials 14 (2) (2021) 407.
[46] V. Maier-Kiener, K. Durst, Advanced nanoindentation testing for studying strain-rate sensitivity and activation volume, JOM 69 (11) (2017) 2246–2255.
[47] V. Maier et al., An improved long-term nanoindentation creep testing approach for studying the local deformation processes in nanocrystalline metals at room and elevated temperatures, J. Mater. Res. 28 (9) (2013) 1177–1188.
[48] V. Maier et al., Nanoindentation strain-rate jump tests for determining the local strain-rate sensitivity in nanocrystalline Ni and ultrafine-grained Al, J. Mater. Res. 26 (11) (2011) 1421–1430.
[49] D. Singh et al., Micropillar compression of Al/SiC nanolaminates, Acta Mater. 58 (20) (2010) 6628–6636.
[50] B. Lucas, W. Oliver, Indentation power-law creep of high-purity indium, Metall. Mater. Trans. A 30 (3) (1999) 601–610.
[51] S. Schröders et al., Room temperature deformation in the Fe_7Mo_6 μ-Phase, Int. J. Plast 108 (2018) 125–143.
[52] K. Momma, F. Izumi, VESTA 3 for three-dimensional visualization of crystal, volumetric and morphology data, J. Appl. Cryst. 44 (6) (2011) 1272–1276.
[53] S. Luo et al., Micro-compression of Al_2Ca particles in a Mg-Al-Ca alloy, Materialia 21 (2022) 101300.
[54] R. Schiltz Jr, J. Smith, Elastic constants of some M Al2 single crystals, J. Appl. Phys. 45 (11) (1974) 4681–4685.
[55] W.-Y. Yu et al., First-principles investigation of the binary AB2 type Laves phase in Mg–Al–Ca alloy: Electronic structure and elastic properties, Solid State Sci. 11 (8) (2009) 1400–1407.
[56] K.L. Johnson, K.L. Johnson, Contact mechanics, Cambridge University Press, 1987.
[57] A. Fischer-Cripps, P. Karvankova, S. Vepřek, On the measurement of hardness of super-hard coatings, Surf. Coat. Technol. 200 (18–19) (2006) 5645–5654.
[58] W.D. Nix, H. Gao, Indentation size effects in crystalline materials: a law for strain gradient plasticity, J. Mech. Phys. Solids 46 (3) (1998) 411–425.
[59] P. Howie et al., Softening non-metallic crystals by inhomogeneous elasticity, Sci. Rep. 7 (1) (2017) 1–9.
[60] C. Marichal et al., 110 Slip with 112 slip traces in bcc Tungsten, Sci. Rep. 3 (1) (2013) 1–7.
[61] H. Van Swygenhoven, S. Van Petegem, In-situ mechanical testing during X-ray diffraction, Mater Charact 78 (2013) 47–59.
[62] J. Zhu et al., Point defects in binary Laves phase alloys, Acta Mater. 47 (7) (1999) 2003–2018.
[63] K. Eichler et al., Änderung von Verformungseigenschaften der intermetallischen Verbindung $MgZn_2$ im Homogenitätsbereich, Krist. Tech. 11 (11) (1976) 1185–1188.
[64] R. Peierls, The size of a dislocation, in: Selected Scientific Papers Of Sir Rudolf Peierls: (With Commentary), World Scientific, 1997, pp. 273–276.
[65] Forbes, R.G., *The prediction of zero-barrier evaporation field: Datasheet from Condensed Matter · Volume 45B: "Physics of Solid Surfaces" in SpringerMaterials (https://doi.org/10.1007/978-3-662-53908-8_158)*, G. Chiarotti and P. Chiaradia, Editors., Springer-Verlag GmbH Germany.
[66] M. Spittel, T. Spittel, Influence of chemical composition and forming conditions on flow stress, in: Part 3: Non-ferrous Alloys-Heavy Metals, Springer, 2016, pp. 18–64.
[67] S. Korte et al., Deformation of silicon–insights from microcompression testing at 25–500 C, Int. J. Plast 27 (11) (2011) 1853–1866.
[68] Cottrell, A.H., *The Bakerian Lecture, 1963. Fracture.* Proceedings of the Royal Society of London. Series A. Mathematical and Physical Sciences, 1963. **276** (1364): p. 1-18.
[69] D.C. Palmer, Visualization and analysis of crystal structures using CrystalMaker software, Zeitschrift für Kristallographie-Crystalline Materials 230 (9–10) (2015) 559–572.
[70] H. Conrad, Thermally activated deformation of metals, JOM 16 (7) (1964) 582–588.
[71] P. Paufler, Deformation-mechanism maps of the intermetallic compound $MgZn_2$, Krist. Tech. 13 (5) (1978) 587–590.
[72] P. Paufler, G. Schulze, Plastic deformation of the intermetallic compound $MgZn_2$, physica status solidi (b) 24 (1) (1967) 77–87.
[73] Y. Ohba, N. Sakuma, High temperature-room temperature deformation behavior of $MgCu_2$ laves phase intermetallic compound, Acta Metall. 37 (9) (1989) 2377–2384.
[74] H. Saka et al., Plasticity of single crystals of Fe_2(Dy, Tb) Laves phase at high temperatures, Philos. Mag. A 68 (5) (1993) 871–884.
[75] Z. Xie, et al., Unveiling the mechanisms of motion of synchro-Shockley dislocations. arXiv preprint arXiv:2205.02669, 2022.